IS-T-678

EFFECTS OF TEMPERATURE AND MICROSTRUCTURE ON THE ELASTIC PROPERTIES OF SELECTED Eu_2O_3-HfO_2 COMPOSITIONS

Robert Richard Suchomel

M. S. Thesis Submitted to Iowa State University

Ames Laboratory, ERDA
Iowa State University
Ames, Iowa 50011

Date Transmitted: October 1975

PREPARED FOR THE U. S. ENERGY RESEARCH AND DEVELOPMENT ADMINISTRATION UNDER CONTRACT NO. W-7405-eng-82

DISCLAIMER

Available from: National Technical Information Service
U. S. Department of Commerce
P.O. Box 1553
Springfield, VA 22161

Price: Microfiche $2.25

IS-T-678

Effects of temperature and microstructure on the elastic properties of selected Eu_2O_3-HfO_2 compositions

by

Robert Richard Suchomel

A Thesis Submitted to the
Graduate Faculty in Partial Fulfillment of
The Requirements for the Degree of
MASTER OF SCIENCE

Department: Materials Science and Engineering
Major: Ceramic Engineering

Approved:

In Charge of Major Work

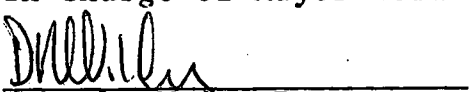

For the Major Department

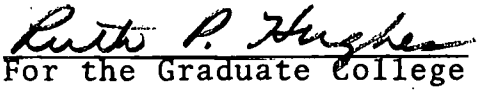

For the Graduate College

Iowa State University
Ames, Iowa

1975

TABLE OF CONTENTS

ABSTRACT*

Europium oxide is presently being tested for use as the control material in future nuclear power reactors. Elastic properties of europia and selected europia-rich compositions of the europia-hafnia system were investigated in this study. The sonic technique was employed to measure elastic moduli from room temperature to 1500°C.

Sintered monoclinic europia specimens were found to have uncommonly low room temperature moduli values and to exhibit hysteresis between heating and cooling curves because of the presence of microcracks caused by thermal expansion anisotropy. Fine grained hot pressed europia as well as sintered specimens that contained at least 6 mole % hafnia did not exhibit these characteristics. Photomicrographs revealed that grain growth suppression was produced by and related to the amount of hafnia introduced. Hysteresis loops in the moduli versus temperature measurements were exhibited only by those specimens for which the average grain size was in excess of a critical value of 8 μm.

Dilatometer measurements indicated that thermal expansion was relatively constant over the compositional range of interest.

---

*U.S. ERDA Report IS-T-678. This work was performed under contract W-7405-eng-82 with the U.S. Energy Research and Development Administration.

INTRODUCTION

Of critical importance in any nuclear reactor is the material which controls the fission rate. Several of the lanthanides are among the select group of elements capable of regulating the fission process by absorbing energetic neutrons. Europium, especially has been of great interest in this area and has had many applications as a control material. In its oxide form, europium is currently under evaluation for use in the next generation of power reactors. Both the Liquid Metal Fast Breeder Reactor (LMFBR) and the Gas Cooled Fast Reactor (GCFR) may utilize this rare earth element (1).

For these anticipated uses to be realized, much more must be learned of the physical properties of the oxide. This includes, in particular, the elastic properties examined in this study. Other investigators have revealed phenomena which may diminish the appeal of europia for nuclear applications. These reports include the tendency of europia toward extreme grain coarsening (2), poor resistance to aqueous attack (3), and an abnormally low Young's modulus (4). This study while increasing knowledge of the physical properties of europia also explores the possible benefits to be obtained by doping europia with another oxide. A logical choice, in view of the proposed applications, is hafnium oxide, another material of great nuclear interest.

The objective of this investigation is twofold: first,

to study Young's modulus, shear modulus, and thermal expansion of monoclinic Eu_2O_3 and selected Eu_2O_3-HfO_2 compositions; and second, to determine the relationship of these properties to microstructure.

LITERATURE SURVEY

Applications of Eu_2O_3 and HfO_2 as Nuclear Materials

Four active elements are commonly used in absorber materials in present day water reactors. These are boron, hafnium, europium, and a mixture of silver-indium-cadmium (5). Each is particularly suited for specific applications. Both europium and hafnium, the elements of interest in this work, are first choices in certain reactors (6). Europium oxide, dispersed in a stainless steel matrix, has been extensively utilized in U.S. Army reactors including the APPR, SM and PM programs (7).

Metallic europium is not commonly employed due to its poor resistance to corrosion attack. It does not possess the excellent corrosion resistance of hafnium which permits this element to be used in water reactors without cladding. The high oxidation potential of metallic Eu eliminates any possible unclad applications (3). In its sesquioxide state, poor aqueous corrosion behavior again prohibits any contact between it and the coolant water (3).

To insure reliability in U.S. Army reactors, Eu_2O_3 dispersions in stainless steel are used (7). These dispersions, while demonstrating excellent neutron control, are extremely expensive and not considered feasible for large power reactors (5).

Because of the attractive nuclear properties of europium considerable interest has been generated in attempts to en-

hance its stability and corrosion resistance. Leitten and Beaver (3) discuss successful stabilization of europium oxide by reaction with a variety of secondary oxides. Compounding Eu_2O_3 with either Al_2O_3, MoO_3, or TiO_2 yields improved corrosion behavior, with the composition $Eu_2O_3 \cdot 2TiO_2$ being exceptionally attractive.

It has been suggested by Ray (7) that stabilization of europium oxide be attempted with another accepted absorber; proposing the formation of either europium boride or $Eu_2O_3 \cdot 2HfO_2$. Large amounts of hafnia have been shown to significantly reduce the hot water attack on several rare earth oxides (8). The ionic radii of Eu^{3+} (.95Å) and Hf^{4+} (.81Å) are similar enough to expect a wide range of solid solution and fluorite structure (9), a system easily characterized and convenient to work with.

In contrast to the physical concerns discussed above, the candidate absorber materials for the fast breeder reactor program are selected almost exclusively because of their nuclear properties. Very few isotopes have the absorption cross section needed to control a neutron spectrum that reaches to above 10 Mev with a peak flux at 200 Kev (10). Only boron, tantalum, and europium are considered to have adequate cross sections for use in fast reactors. Hafnium, mentioned earlier, does not meet this stringent criterion since 90% of its absorption occurs between 1 and 10 ev (11). However, it is

somewhat effective to above 4 Kev so it could be used as an additive to capture thermal neutrons.

Among the three acceptable control materials there is only one, europium, which possesses a series of consecutive isotopes, each of which has a high neutron absorption cross section, so that all isotopes are useful as control materials. Moreover, the capture of a neutron does not destroy the worth of an atom. Capture is accompanied only by a one unit increase in the mass number of the atom. Thus each atom retains neutron capture potential until it either reaches the end of the isotopic chain or decays by beta emission into an isotope of gadolinium. Data taken from McMasters and Gschneidner (12) is tabulated in Fig. 1. It lists the isotopes as well as the natural occurrence, capture cross section, and decay mode of each. The existence of consecutive nuclides provides the element with a reactivity lifetime that is superior to that of the other two candidates.

A cursory economic analysis places Eu_2O_3 in a very unfavorable position. Europium sesquioxide is currently valued at $365/lb, more than ten times the price of an alternative material, B_4C. However, a list price for B_4C of $20/lb is only for naturally occurring boron. To highly enrich the carbide in B^{10}, the only isotope with high neutron capture potential, would increase the price to around $3600/lb (1). The decision to require any enrichment depends of course on

Figure 1. Decay and neutron capture schemes of europium isotopes. The values given after the natural occurring isotopes Eu^{151} and Eu^{153} are the relative abundances. The symbol n designates neutron capture; it is followed by the neutron capture cross-section for thermal neutrons in barns. The symbol β^- indicating beta particle emission is followed by the half-life of the isotope.

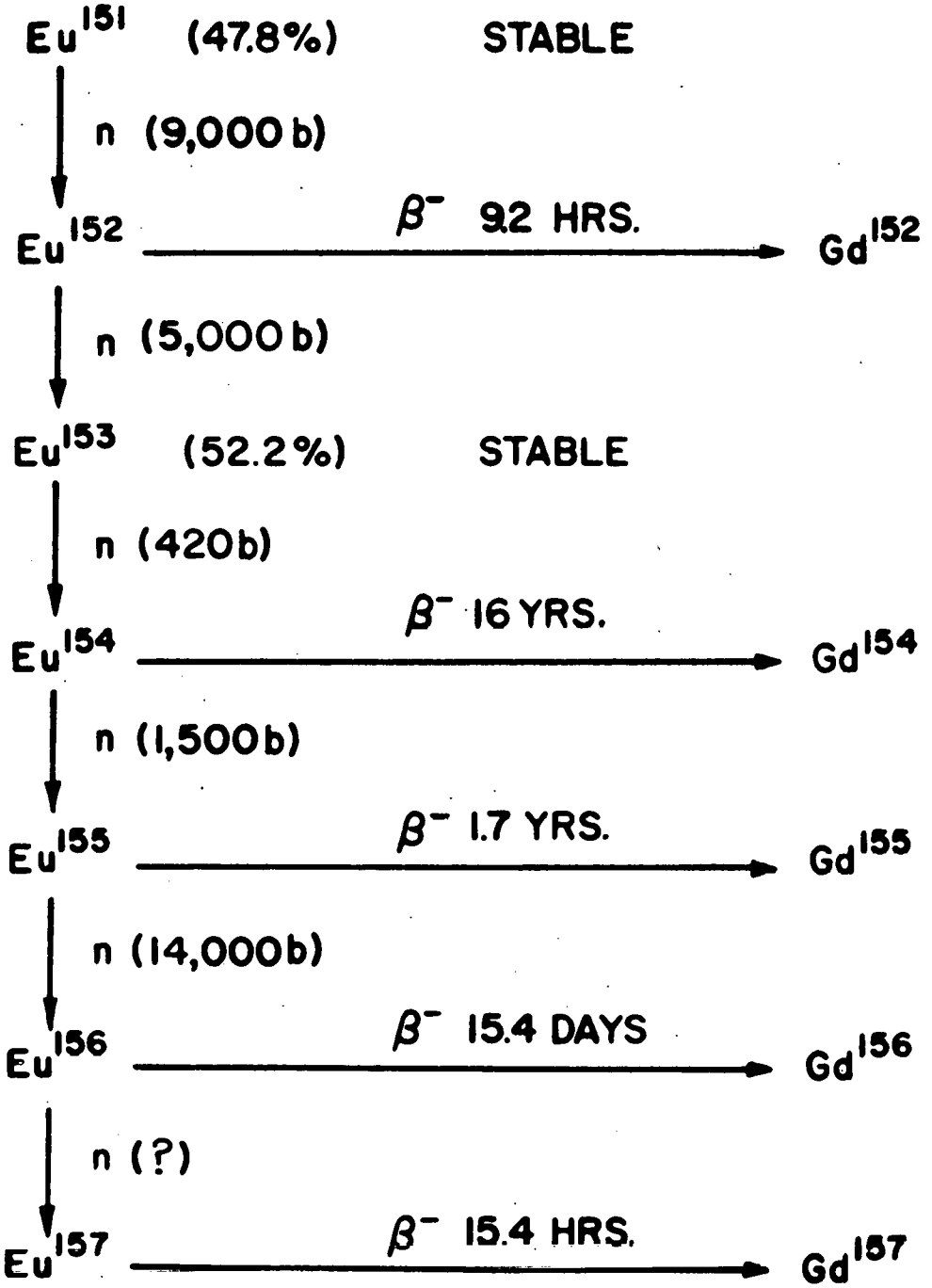
Eu151 (47.8%) STABLE
n (9,000 b)
Eu152
β⁻ 9.2 HRS.
Gd152
n (5,000 b)
Eu153 (52.2%) STABLE
n (420b)
Eu154
β⁻ 16 YRS.
Gd154
n (1,500b)
Eu155
β⁻ 1.7 YRS.
Gd155
n (14,000b)
Eu156
β⁻ 15.4 DAYS
Gd156
n (?)
Eu157
β⁻ 15.4 HRS.
Gd157

performance criteria such as necessary reactivity worth and the useful lifetime of the control element.

Raw material cost is not the sole determinant in an economic evaluation. Gray (1) points out that several other factors have great influence. The nuclear worth per volume of the control material, both as fabricated and after extended core life, determines the number and size of control rods necessary. In this regard Eu_2O_3 performs favorably. Also of interest are the costs associated with the fabrication and assembly of absorber elements. B_4C must be produced by expensive hot press techniques while Eu_2O_3 can be sintered economically using existing UO_2 fabrication procedures (1).

Each of the three candidate materials has certain undesirable characteristics which makes the choice of the prime material more difficult. Tantalum is perhaps the least attractive choice. Its use would insure cooling problems in the reactor after shutdown since its decay heat is very high (1). Massive equipment would also be needed to manipulate tantalum rods because of the high density of the metal.

B_4C, the control material chosen for the first prototype LMFBR, also has very unattractive characteristics. Unlike Eu_2O_3 each boron atom can absorb only one neutron. Thus its worth decreases more rapidly with irradiation than does that of europia (10). The consequences that result from neutron capture are also quite unlike those of Eu_2O_3. Whenever a

boron (B^{10}) atom absorbs a neutron it spontaneously transforms into a lithium atom by the release of an alpha particle. With time, this alpha decay produces a measurable helium pressure within the clad control pin. Heavy cladding and a special plenum chamber are required to insure the integrity of the element.

The candidacy of europia is certainly hampered by the raw materials cost. In an engineering sense however, the more crucial limitation arises from the lack of knowledge about physical properties and operating characteristics. For example, only sketchy information is available on its strength, elastic characteristics, and thermal conductivity. More data must be taken in order to adequately analyze stress and thermal conditions within the control pins.

After considering all these factors, Spenke (13) contends that Eu_2O_3 might well be the optimal absorber material. His measurements of a most important parameter, the worth per unit volume, show europia to be superior to natural boron carbide and both of these to have twice the worth of tantalum.

Physical Properties of Eu_2O_3-HfO_2

The works cited above along with the results of this work suggest that doping Eu_2O_3 with HfO_2 would enhance its attractiveness as a control material. To perform and to analyze the results of any dopant experiments, knowledge of the system is essential. Unfortunately, very little is known concerning the

Eu_2O_3-HfO_2 phase diagram. A study by Radzewitz (14) has shown that a two phase region composed of fluorite and monoclinic structures exists at 1500°C between 56 and 82 mole % Eu_2O_3. Apparently no other structural determinations have been made at other temperatures or compositions.

Even the structural transformations in pure Eu_2O_3 are not clearly understood. Investigators agree that there is a transformation at 1050°C but the reversibility of this transformation is in doubt. Warshaw and Roy (15) found the transformation between the low temperature cubic form and the high temperature monoclinic structure to be reversible. However, Glushkova and Boganov (16) found that once formed, the monoclinic structure is stable at all temperatures. Hoekstra (17), in another work, has reported the transformation to be reversible only in the presence of water as a catalyst.

The physical properties of Eu_2O_3 are almost as poorly characterized as its structure. Curtis and Tharp (4) have prepared the most extensive report of such properties. They have made the only reported elasticity measurements of Eu_2O_3. In their work, room temperature measurements on a few bars of high density yielded Young's modulus values of about 310 Kilobars. Not only has this value never been reproduced, but it is also substantially lower than has been reported for other rare earth oxides. In sharpest disagreement have been investigations by Hunter *et al*. (18,19) on structurally similar rare earth sesquioxides. They have reported room temper-

ature moduli of elasticity values of up to 1400 Kilobars for both Sm_2O_3 and Gd_2O_3.

Mechanical behavior is not the only area in which uncommon values have been reported. Europium is exceptional among the rare earths in atomic structure in that the 4f valence orbitals are exactly half filled. Because of this atomic structure, two oxidation states, a 2+ state as well as the normal 3+ state are possible for europium in its ionic form. Thus the formation of an oxide other than the sesquioxide is conceivable. McCarthy (20) has presented a diagram showing the relative ease with which Eu_2O_3 can be reduced to form Eu_3O_4 or even EuO.

Yet another distinguishing feature of Eu_2O_3 is its tendency toward grain coarsening. Ploetz et al. (2) sintered several rare earth oxides at 1800°C for three hours and then studied the resultant microstructures. They found the average grain size to be 40 μm for Dy_2O_3, 80 μm for Sm_2O_3, 80-120 μm for Gd_2O_3, and 340-550 μm for Eu_2O_3. No explanation to account for this extraordinary grain growth was presented. Incidentally, the excessive grain size found in sintered Eu_2O_3 gives rise to serious concerns about its performance in-reactor. Pasto et al. (21) expressed the fear that large grains in the anisotropic monoclinic structure would lead to intensive intergranular stresses. In Patriarca's (22) report serious concern over the effect of grain size on irradiation

behavior can also be found.

Intergranular Stresses and Microcracks

As a general rule in polycrystalline ceramic materials the elastic properties are not significantly affected by grain size. Wachtman (23) characterizes the elastic moduli as not being "structure sensitive" properties. In a number of materials however, an obvious relation between elasticity and structure has been established. It has been noted by Buessem (24) that extraordinarily low room temperature elastic moduli values are but some of the characteristic features of a material with a strong anisotropy of thermal expansion. His paper cites a number of references in which this and the other unusual properties have been explained on the basis of "internal ruptures and recombinations".

These ruptures or cracks are produced as a body which has no internal stresses at the sintering temperature is cooled. Different contraction rates in each of the principle crystallographic directions of each crystallite produces a complex arrangement of intragranular microstresses as the body cools to room temperature. Stresses generated in thermally anisotropic materials can be quite large; calculations made on the α-uranium structure predict stress to develop at the rate of 360. psi for every degree Celcius the material is cooled (25). Such a concept would appear to be validly applied to Eu_2O_3 which also lacks isotropy.

Of course anisotropy in thermal expansion is not the only mechanism for inducing microcracks. Rapid phase transformations have also been shown to produce internal ruptures. That a reconstructive phase transformation can lead to microcracking has been shown by Ault and Ueltz (26) in their work with unstabilized zirconia. Two-phase ceramic bodies are also subject to microcracking whenever the components have dissimilar thermal expansion coefficients. The relation of such differences to the onset of microcracking has been studied by Hunter and Brownell (27).

If thermal expansion anisotropy induces microcracks in Eu_2O_3, then such cracks should also be seen in other polycrystalline monoclinic rare earth oxides. Hunter et al. (18) performed a temperature study of Young's modulus on samaria and found evidence of microcracking by a small hysteresis loop in their data. A similar investigation of gadolinia by Haglund and Hunter (19) found no such hysteresis but their work was performed on relatively fine grained specimens. Subsequent work on Gd_2O_3 showed pronounced hysteresis in the elasticity curves when specimens with larger grains were tested.[1]

Outside of the lanthanide oxides, microcracking has been clearly shown to be responsible for anomalous behavior in a number of oxides. The phenomenon is most vividly seen in

[1]S. L. Dole. Ames Laboratory, ERDA, Iowa State University, Ames, Iowa. Private communication. May 9, 1975.

Manning and Hunter's (28) report on the elastic behavior of polycrystalline Nb_2O_5. They obtained high temperature Young's moduli for both hot-pressed and sintered compacts. For the smaller-grained (8 μm) hot-pressed material, Young's modulus decreased, linearly with temperature, while the larger grained (20 μm) sintered specimens showed the effects of internal microcracking. Sintered materials exhibited unusually low room temperature values of Young's modulus and a hysteresis between heating and cooling curves. Young's modulus actually increased over 250 percent from room temperature to 1000°C. They explained this phenomenon by attributing the increase to healing of the microcracks.

Other evidence of microcracking was found by Bush and Hummel (29) in the mechanical behavior of β-eucryptite. A similar hysteresis was found in the behavior of Young's modulus in this material which also has anisotropic thermal expansion. Again crack healing at high temperature was given as the reason for this hysteresis.

Stress calculations show that grain size should not be an influence on either the onset or extent of internal microcracking (25). However the literature on thermally anisotropic materials clearly shows that fine-grained materials display none of the unusual properties associated with microcracking while large-grained ones do.

Titanates have frequently been studied to obtain insight into this question of the influence of grain size. Matsuo and

Sasaki (30) blended additives into $PbTiO_3$ to determine the effects, particularly the effect on strength. Here again the existence of microcracking was dependent on grain size. Additives produced mechanically strong $PbTiO_3$ not by depressing thermal expansion anisotropy but rather by inhibiting grain growth. Investigation of Young's modulus in another titanate, $MgTi_2O_5$, by Bush and Hummel (31) also yielded the hysteresis characteristic of internal stress release and cracking. The study of magnesium dititanate was expanded by Kuszyk and Bradt (32) to show more closely the influence of grain size. They observed a critical grain size of 3 μm; that is, only samples with grains larger than 3 μm displayed the unusual characteristics seen by Bush and Hummel (31).

Based on their results Kuszyk and Bradt proposed an energy criteria which must be fulfilled before microcracking could occur. This energy criterion is distinct from and in addition to the micro stress considerations which have been shown to be independent of grain size. Such an energy consideration for microcracking is analogous to Hasselman's (33) description of elastic energy as a critical quantity in causing thermal shock fracture. Microstresses existing within the material can be described by a strain energy function taken over the volume of the body. However if this strain should be relaxed by the formation of microcracks then at least some of this energy is converted into surface energy, the amount

determined by the area of the fracture surfaces formed. Thus there is a relationship between the two energy functions. A critical grain size is expected to be the determinant just as size controls nucleation of crystallites in a glass melt where surface and volume energies also compete. Mathematically Kuszyk and Bradt express these energy terms in a single grain by:

$$\text{Energy} = -(SE)\ell^3 + (\gamma_f)\ell^2$$

where SE is the strain energy per unit volume,

γ_f is the average fracture surface energy, and

ℓ is the grain size.

Differentiating this with the assumption that neither energy is a function of grain size and setting equal to zero yields:

$$\ell_{crit} = \frac{2\gamma_f}{3(SE)}$$

where ℓ_{crit} is the minimum grain size for crack formation. The authors feel that the concepts of an energy criterion and critical grain size will aid in the understanding of micro-cracked materials.

EXPERIMENTAL PROCEDURE

Specimen Preparation and Characterization

Both materials used in this project were received as aqueous solutions (Ames Laboratory Rare Earth Separation Group). The europium had been extracted from xenotime ore through the use of ion exchange columns. This process involves passing the xenotime solution through the columns using an organic chelating agent as an elutant. The purified europium was then precipitated and calcined to the oxide to remove the organics. Following this step the supplier redissolved it in dilute hydrochloric acid. The hafnium originally of commercial grade, was purified by the same source. An organic batch extraction process was used, followed by precipitation in ammonium hydroxide. Finally the material was put back into solution again using hydrochloric acid as the solvent.

After receiving the solutions from the supplier, a qualitative analysis was obtained on each (Ames Laboratory Spectrographic Analysis Group). Results of these analyses are presented in Table 1 and Table 2.

In this study Eu_2O_3 was doped with HfO_2 in increments of 2 mole percent from 0 m/o thru 10 m/o. Several pure Eu_2O_3 bars of varying porosity as well as two of comparable density at each dopant level were to be made and tested. Material for the compositions of interest was prepared by pipetting together measured amounts from each solution, the solutions

Table 1. Spectrographic analysis of impurities in europium solution

Element	Concentration (ppm)	Element	Concentration (ppm)
Al	ND[a]	Ni	ND
Ca	100	Si	2000
Ce	ND	Sm	ND
Cu	ND	Tb	ND
Fe	1	Ti	ND
Gd	ND	Y	ND
Mg	150	Zr	ND

[a]Not detected.

Table 2. Spectrographic analysis of impurities in hafnium solution

Element	Concentration (ppm)	Element	Concentration (ppm)
Al	50	Ni	ND[a]
Ca	500	Si	2000
Cu	150	Ta	ND
Fe	ND	Ti	ND
Mg	150	Zr	320
Nb	ND		

[a]Not detected.

having previously been standardized (Ames Laboratory Analytical Chemistry Group). After thorough stirring each batch was co-precipitated into an aqueous ammonia solution. The precipitate was separated by filtration. While still contained in filter paper the precipitate was washed with a dilute ammonium hydroxide solution to remove residual chlorides. When chloride was no longer detectable the filtrate was transferred to a beaker, covered, and dried at 100°C to remove mechanical water from the hydroxide.

To prepare the materials for specimen fabrication the hydroxide was crushed, calcined at 900°C to form the oxide, slugged to 30,000 psi in an isostatic press, and reground to pass a 200 mesh sieve. Green compacts were formed by mechanically pressing the powder in a double acting steel die having a rectangular cavity of 8.25 cm x 0.56 cm. A pressure of 6,000 psi was used in this operation. Rectangular prisms thus formed were further densified with the use of an isostatic press. The bars were sealed in rubber containers and pressed isostatically to 30,000 psi. The pressures given here were used whenever possible. Certain compacts cracked extensively after such pressings, however. Such difficulties, apparently associated with adsorption of atmospheric gases, were remedied by pressing at lower pressures; mechanically at 1,500 psi, then isostatically at 7,000 psi. Similar adsorption problems have been reported by other authors (21,34).

Firing of all bars was done in an oxidizing atmosphere through the use of a gas fired muffle furnace. Each bar was initially sintered at 1800°C for one hour. After elasticity vs temperature curves were generated, most bars were refired to 1900°C for another hour. The oxidizing air atmosphere within the muffle chamber eliminated any concern over reduction of the sesquioxide.

One specimen used in this work was not fabricated in the manner described above. This specimen was already densified when it was received from an outside source (Oak Ridge National Laboratory). It is unique in this study in that it was prepared by hot pressing rather than sintering. This specimen was formed from commercial (Molycorp) cubic Eu_2O_3 powder which had been slugged to 20,000 psi and crushed to -20 mesh. Actual hot pressing was done by holding the pressure constant at 6000 psi while the temperature was held first at 1125°C for one hour, then increased to 1300°C in ten minutes and held at this higher temperature for another hour. Following hot pressing stoichiometry was restored by heating the sample in air at 1000°C for three hours.

Following firing, a surface grinder employing a silicon carbide wheel was used to shape the sintered specimens into rectangular prisms with a dimensional tolerance of $\pm$ 0.001 cm. The dimensions of a typical specimen after shaping were 5.5 cm x 0.7 cm x 0.2 cm. The bulk density of each bar was deter-

mined from its mass and dimensions. X-ray diffraction was employed to determine the crystallographic form of each specimen. Other characterization included reflecting light and scanning electron microscopy to analyze microstructures. Average grain sizes were computed using the linear intercept technique and correction factor from Fullman (35).

Elasticity Measurements

The Forster (36) or sonic resonance technique was used to determine elastic moduli in this study. This procedure follows that outlined by Spinner and Tefft (37). Detailed descriptions of the actual equipment used in this work have been written by several authors, most notably Manning (38) and will not be repeated here. Basically the technique involves measuring sonic resonance frequencies of the specimen to determine Young's and shear moduli as well as Poisson's ratio. To perform resonance measurements on a specimen, it was suspended by cotton thread from two devices, one a magnetic record cutting head (driver) and the other a phonograph cartridge (pickup). Through appropriate electronic instrumentation, i.e. variable frequency oscillator, power amplifier, oscilloscope, and vacuum tube voltmeter, a signal was generated and amplified, fed into the test specimen as a mechanical vibration, and monitored after it passed through the specimen. A diagram of the equipment arrangement is available in Fig. 2. With this technique, resonant frequencies were easily identi-

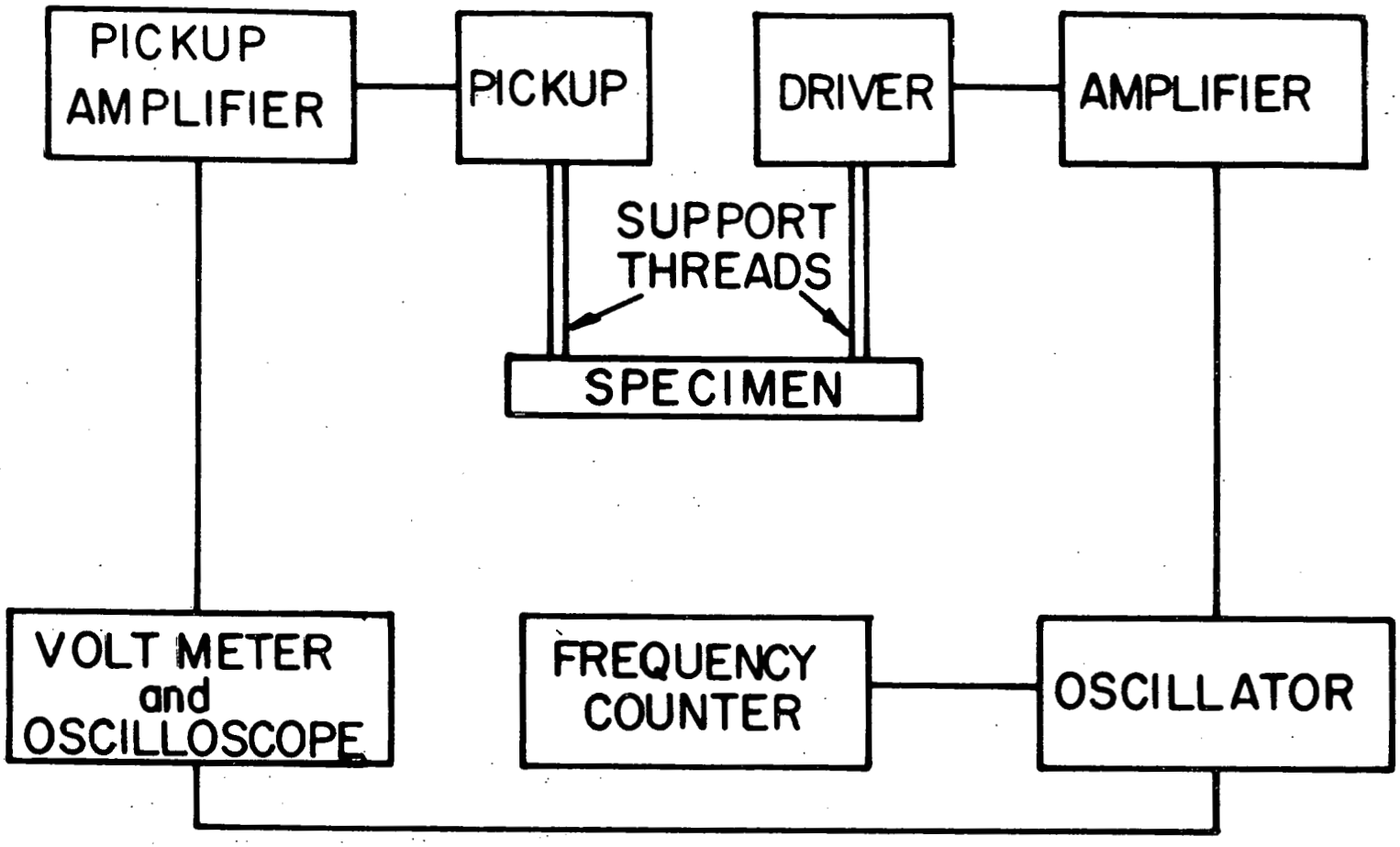

Figure 2. Block diagram of resonant frequency apparatus

fiable as being those frequencies at which signals were easily transmitted through the test bar. The mode of resonance was determined by probing the bar during excitation to observe the location of the nodal planes. Diagrams of the resonance vibrational modes, flexural and torsional, can be seen in Fig. 3.

Measurements at other than room temperature were made by suspending the specimen with carbon yarn in a carbon rod resistance furnace. The specimen, furnace, cutting head, and phonograph cartridge were covered under a bell jar and a pressure of less than 1×10^{-5} torr was drawn. Temperature in the manually controlled furnace was determined by use of a Pt-Pt 10% Rh thermocouple and a digital voltmeter.

To convert resonance data into moduli, the equations of Pickett (39) were used but in a form given by Hasselman (40). Shear modulus for a prism of rectangular cross section can be obtained directly from the equation:

$$G = \frac{4LRmf_t^2}{S},$$

where G is the shear modulus,

L is the length of the test specimen

m is the mass of the test specimen

f_t is the resonant frequency of the fundamental mode of torsional vibration

S is the area of the cross section, and

R is a shape factor given by:

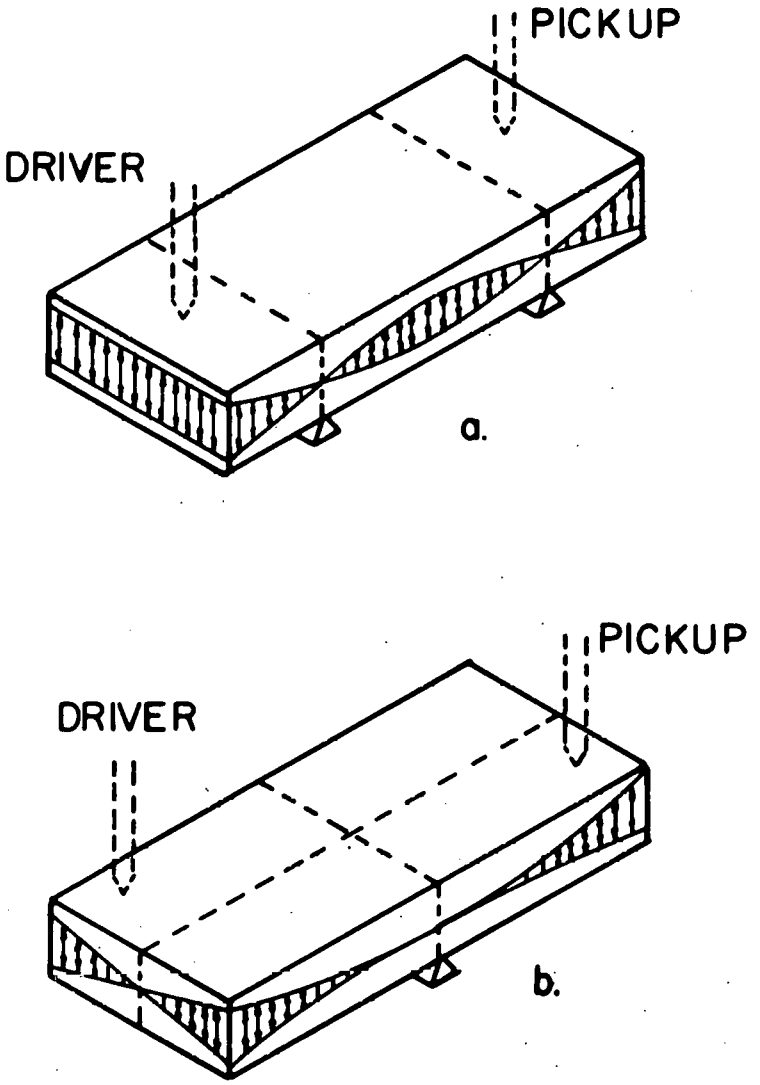

Figure 3. Fundamental modes of resonant vibration in rectangular prisms (from Hasselman (40))
a. Flatwise flexural vibration
b. Torsional vibration

$$R = \frac{A/B + B/A}{4A/B - 2.52(A/B)^2 + .21(A/B)^6}$$

where A is the length of the shorter side and

B is the length of the longer side of the cross section.

In quite similar fashion, Young's modulus for a rectangular prism can be calculated from the equation:

$$E = 0.94645 \frac{C\ m\ f_f^2}{B}$$

where E is Young's modulus

f_f is the resonant frequency of the fundamental mode of flexural vibration, and

C is a shape factor defined by:

$$C = [1+6.5850(1+0.0752\mu+0.8109\ ^2)(A/L)^2 - \frac{8.340(1+0.2023\mu+2.173\mu^2)(A/L)^4}{1 + 6.338(1+0.14081\mu+1.536\ ^2)(A/L)^2} - 0.86806(A/L)^4](a/L)^{-3}$$

where L is the length of the test specimen, and

μ is Poisson's ratio.

Since this second shape factor involves Poisson's ratio, a third equation:

$$\mu = \frac{E}{2G} - 1$$

is required for solution. Once the shear modulus is known, an initial value for μ can be assumed and the two equations

solved in a circular manner until the desired precision is obtained. If torsional frequency and hence shear modulus cannot be determined for a particular prism, then Poisson's ratio from a similar specimen can be assumed in evaluating Young's modulus since a small error in μ has only a minimal effect on the calculation (41).

Marlowe and Wilder (42) studied the experimental error involved in determining elastic moduli by the sonic technique. At room temperature the overall error should be less than 1.3% with dimensional inaccuracy contributing the largest error. Spinner et al. (41) stated that Young's modulus should be exact to four significant digits with this method.

To correct moduli for the effects of thermal expansion at elevated temperatures an equation from Hasselman (40) was used:

$$M_t = M_o \frac{f_t^2}{f_o^2} \frac{1}{(1+\alpha\Delta T)}$$

where M_t is either modulus at temperature t

M_o is the same modulus at room temperature

f_t is the resonance frequency at temperature t

f_o is the resonance frequency at room temperature

α is the coefficient of linear thermal expansion

ΔT is the temperature difference between temperature t and room temperature.

Secondary Testing

To more fully characterize the various compositions studied, tests of other physical properties were made. Thermal expansion data were obtained at each composition. In addition, specimens were tested to obtain a qualitative measure of resistance to boiling water attack.

Linear thermal expansion measurements were made with a commercial dilatometer (Brinkmann model TD IX). A linear variable differential transformer in contact with the specimen through an alumina push rod measured length changes as the specimen was heated in an alumina tube. An electric resistance furnace with an air atmosphere was used to heat the specimen. Temperature was measured with a Pt-Pt 10% Rh thermocouple positioned close to the specimen. To maintain consistency with the expansion runs, dilatometer measurements were in every instance made before the specimen was reheated to 1900°C.

Boiling water attack of the specimens was observed by boiling small rectangular sections of each composition. The time taken for sample disintegration was noted. The average dimensions of such pieces were about 0.2 cm x 0.7 cm x 0.7 cm. Because of the destructive nature of this experiment it was undertaken only when other forms of analysis had been completed and hence was performed after the specimens had been refired to 1900°C.

RESULTS AND DISCUSSION

Elastic Properties of Monoclinic Eu_2O_3

In any experiment, the effects produced by altering certain parameters cannot be ascertained until comparison to a control or reference state is made. In this study such comparisons are most logically made with pure europia. The elastic properties of monoclinic europia will thus be reported first. Figure 4 and Appendix A show the behavior of Young's modulus as a function of temperature for several specimens. Most striking in these results is the lack of similarity among the four curves. Three of these plots were generated from sintered europia, while the other was obtained from the hot pressed specimen.

Before detailing the contrasting qualities of the two types of specimens, a brief introduction to the usual porosity and temperature dependency of Young's modulus is appropriate. The vertical arrangement of the curves in Fig. 4 is dependent on porosity. Other rare earth oxides (43), and in fact most polycrystalline refractory materials, display porosity dependence for Young's modulus. Both Spriggs (44) and Hasselman (45) have introduced equations to express this effect. While the mathematical functions of these nonlinear equations differ, both agree that the elastic modulus of a material should increase as the porosity decreases. Unfortunately, theoretical equations are of little use in this particular

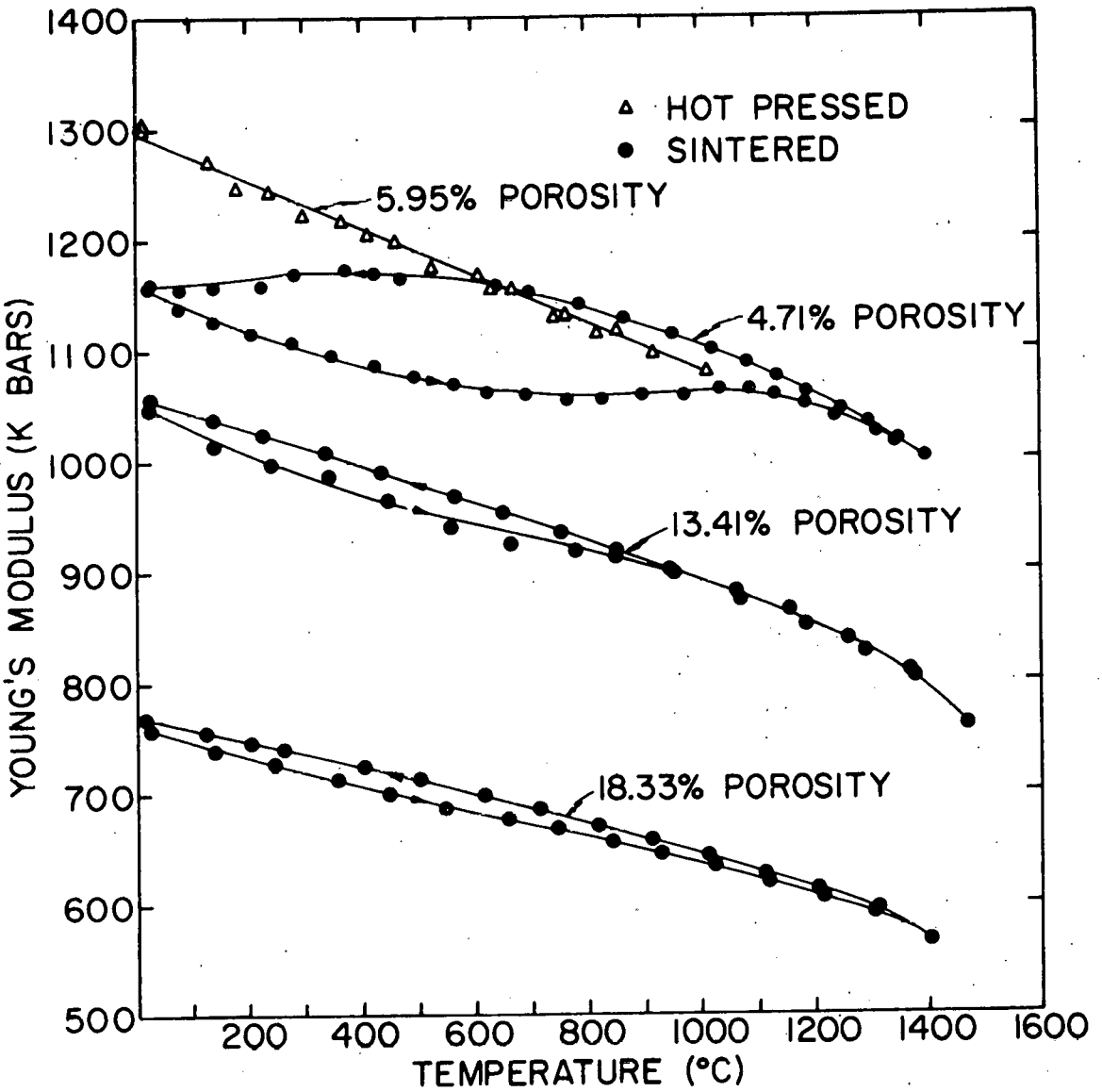

Figure 4. Elevated temperature Young's modulus for sintered and hot-pressed europium oxide

study since several of the curves have unusual shape and are not single-valued with temperature.

Figure 4 also shows how Young's modulus is affected by temperature. Wachtman and Lam (46) after studying a variety of refractory materials concluded that Young's modulus should decrease approximately linearly with increasing temperature. This decrease is caused by thermal expansion; increased bond lengths between atoms produce decreased bond strengths. Such a steady linear decrease is quite evident for the hot pressed material. The loops which depict the behavior of sintered europia specimens fail however, to show such linearity. Figure 4 shows that at very high temperature, above 1300°C for europia, a change is found in temperature dependency. This feature, inherent in polycrystalline ceramics, is caused by high temperature grain boundary slip (47).

Since the Young's modulus of the hot pressed specimen follows the linear temperature dependence predicted by Wachtman and Lam (46), it can be assumed that these data are representative of normal crack-free material. This assumption allows comparison of unusual features of sintered specimens by comparing them to the hot pressed normal material.

This comparison is best accomplished using the sintered specimen of lowest porosity (porosity = 4.71%) since its density is nearly the same as that of the hot pressed specimen (porosity = 5.95%). The major difference between these two

curves is that the sintered specimen does not show linearity but rather a loop composed of two distinct segments with a hysteresis between them. As a result of the porosity dependence discussed earlier, the less porous sintered specimen should have a higher Young's modulus than the hot pressed specimen. Instead, at room temperature, the sintered specimen exhibits a lower modulus. This abnormally low room temperature value plus the already mentioned hysteresis loop between the heating and cooling segments are precisely the characteristics listed by Buessem (24) as being indicative of microcracking.

The development of internal cracking in the sintered specimens and its effect on Young's modulus can be seen by analyzing what occurs along various portions of the modulus loop. Again the least porous sintered specimen shown in Fig. 4 is best used to show these effects. At very high temperature (above 1300°C), the modulus of the sintered specimen is linear, reversible, and shows the correct porosity relationship with respect to the extrapolated curve for the hot-pressed specimen. Since reversible linearity and the proper porosity dependence are observed, there is no reason to suspect that microcracks exist in this temperature region. Here the anisotropic thermal expansion which accompanies heating has relieved enough stress within individual grains to allow the cracks to heal.

As the temperature is decreased however stresses induced by anisotropy in thermal contraction again begin to build within the grains. Near 1200°C, the deviation from high temperature linearity indicates that microcracks are developing. With continued cooling deviation from an extrapolated line passing through the high temperature data increases. Such deviation shows that microcracking becomes more severe as the temperature is lowered. The slope of the cooling curve shows that at low temperatures internal rupturing completely offsets the temperature effect.

During the heating cycle the opposite effect is observed. Initial heating from room temperature produces a linear decrease in Young's modulus with temperature. As temperature is increased to above 500°C some deviation from linearity is again observed. Here the modulus begins to turn upward as microcracks heal. The curve shows the range of crack healing (500°C to 1300°C) and notes the temperature (1300°C) at which the crack free state is again attained.

Data taken on the other sintered specimens support this description although microcracking is probably not as extensive since these specimens have greater porosity; porosity which provides space for the relief of anisotropic thermal expansion stresses.

The Young's modulus versus temperature curves plotted in Fig. 4 and subsequent figures were found to be reasonably

reproducible. However the room temperature moduli values obtained immediately after sintering or refiring were usually not consistent with those obtained after high temperature testing. Room temperature values for pure sintered europia were found to increase by as much as 10% after the first high temperature elasticity measurements. Similar increases were noted at other compositions where microcracking was evidenced. A plausible explanation for this effect can be made considering the difference in cooling behavior found in the sintering and elasticity measurement furnaces. The rapid uncontrolled cooling from the sintering temperatures was quite different from the deliberate controlled temperature changes made during the elasticity study. Microcracking could easily have been intensified by the more rapid crystal contractions accompanying the faster cooling rates. These cracks would of course all heal during the first high temperature elasticity study allowing a different less severe microcrack system to develop on recooling.

It has already been mentioned that an equation to express the effect of porosity on Young's modulus cannot be developed from the sintered specimens because of the microcracking phenomenon. However an estimate of the effect of porosity can be made using the modulus value of the hot pressed specimen. Several investigators (19,48) of the elastic properties of rare earth oxides have concluded that a linear equation fits the data and expresses the porosity effect as well as or

better than the nonlinear equation proposed by either Spriggs (44) or Hasselman (45). This linear equation is of the form:

$$M = M_o(1-bP),$$

where M is either elastic modulus,

M_o is that modulus at zero porosity,

P is the volume fraction porosity, and

b is an experimentally determined constant.

Hasselman and Fulrath (49) theoretically calculated a value of b equal to 2.0 from equations describing the effects of spherical porosity on the various elastic moduli. Wachtman (50) has shown the porosity effect on a variety of oxides to be characterized by slopes of near 2.0. More importantly, Manning et al. (48) observed similarly valued constants in their study of several rare earth oxides.

By assuming a value of 2.0 for the constant in the linear equation and using the room temperature moduli values (E = 1301 Kbars, G = 515 Kbars) of the hot pressed specimen (P = 0.0595), estimated values for both Young's and shear modulus of theoretically dense crack free monoclinic europia can be calculated. Estimated values of E_o (1477 Kbars) and G_o (584 Kbars) were thus obtained. These values lie roughly midway between the linearly extrapolated room temperature moduli values obtained for the two adjacent rare earth oxides, Sm_2O_3 (E_o = 1450 Kbars, G_o = 548 Kbars) (18), and Gd_2O_3 (E_o = 1503 Kbars, G_o = 588 Kbars) (19). Such consistency gives added

significance and confidence to the crack-free moduli values estimated for Eu_2O_3.

Elastic Properties of Eu_2O_3-HfO_2 Compositions

A number of specimens, all identically prepared but of varied compositions, were fabricated and tested in an effort to understand and control internal microcracking. The following plots of Young's modulus, Figs. 5-10, show the consequences of doping Eu_2O_3 with small quantities of HfO_2. Each successive figure illustrates the effect of increased dopant: Fig. 5, 0 mole % HfO_2; Fig. 6, 2 mole % HfO_2; Fig. 7, 4 mole % HfO_2; Fig. 8, 6 mole % HfO_2; Fig. 9, 8 mole % HfO_2; Fig. 10, 10 mole % HfO_2. All moduli values determined in this study are tabulated in Appendix A.

Each figure shows the elastic moduli of a single specimen tested after sintering (1800°C) and again after the reheat treatment (1900°C). Duplicate specimens were similarly tested for each composition except 8 mole % HfO_2 and showed essentially the same results.

Young's modulus of a pure Eu_2O_3 specimen is presented in Fig. 5. Both loops in Fig. 5 show similar hysteresis although the room temperature value is decreased after refiring of the specimen (bottom loop). This suggests microcracking to be more severe following the second heat treatment. The small discrepancy at very high temperature is in agreement with and explainable by the densification which occurred during the

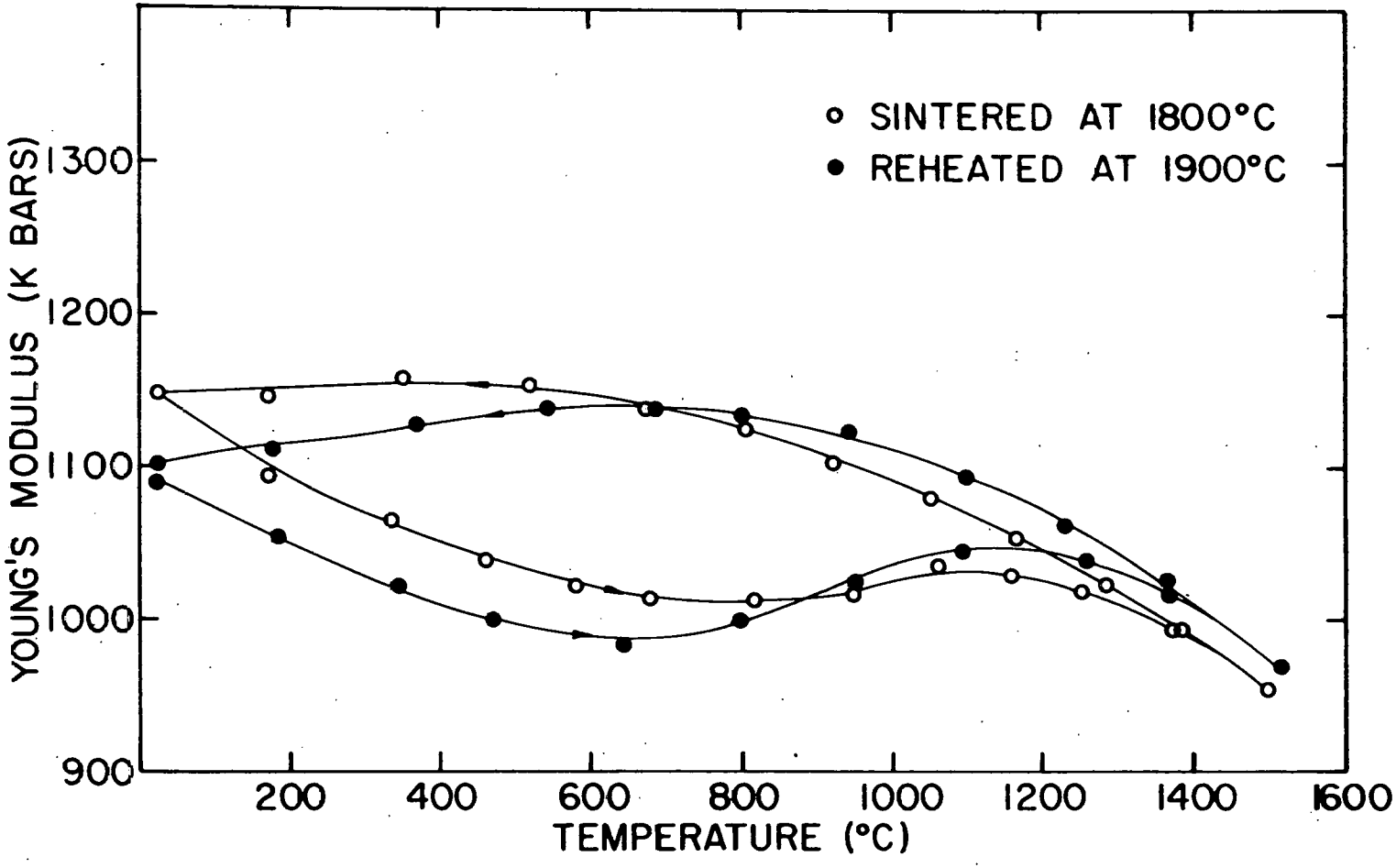

Figure 5. Elevated temperature Young's modulus (heating and cooling) of 100 mole % Eu_2O_3-0 mole % HfO_2

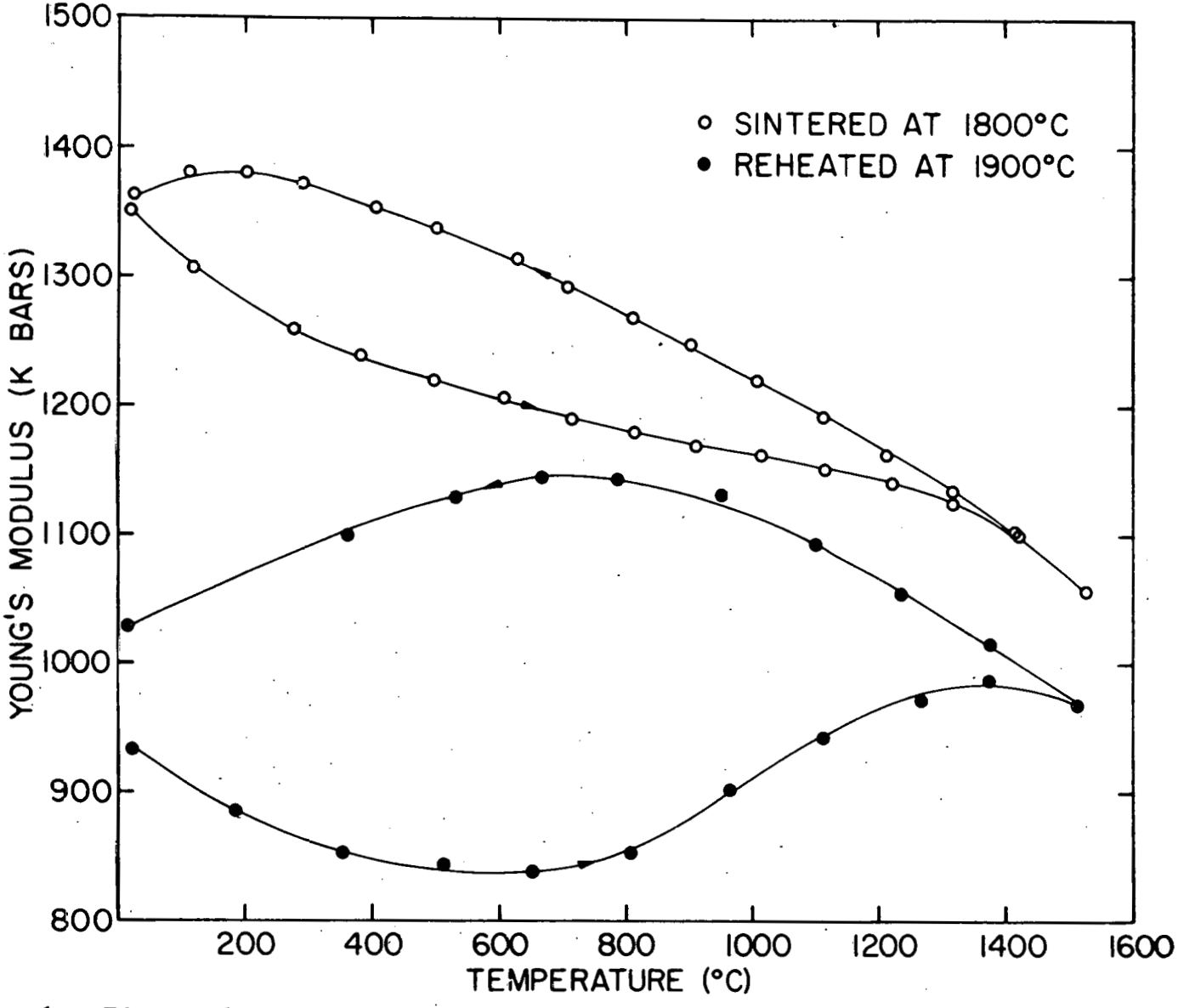

Figure 6. Elevated temperature Young's modulus (heating and cooling) of 98 mole % Eu_2O_3-2 mole % HfO_2

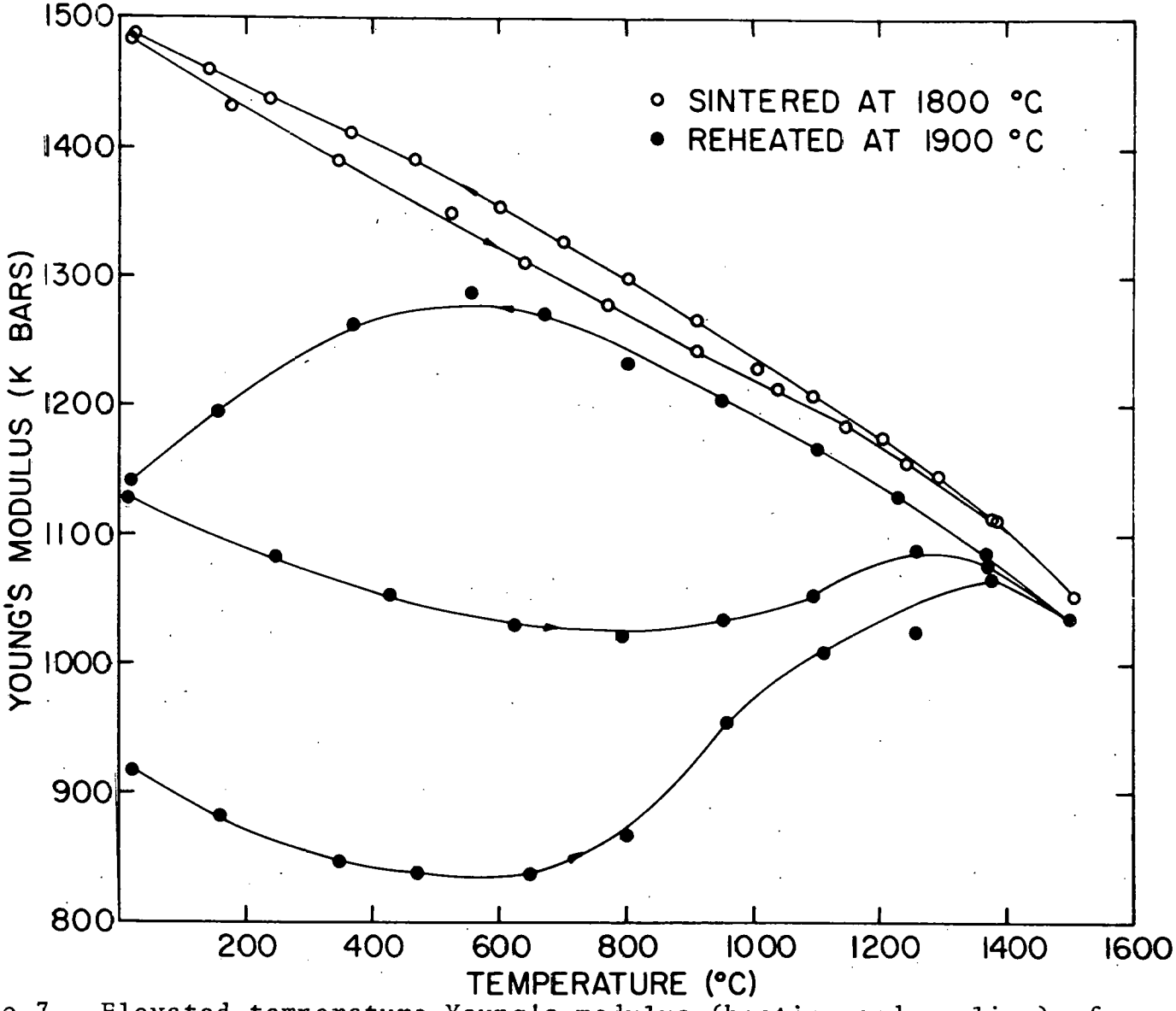

Figure 7. Elevated temperature Young's modulus (heating and cooling) of 96 mole % Eu_2O_3-4 mole % HfO_2

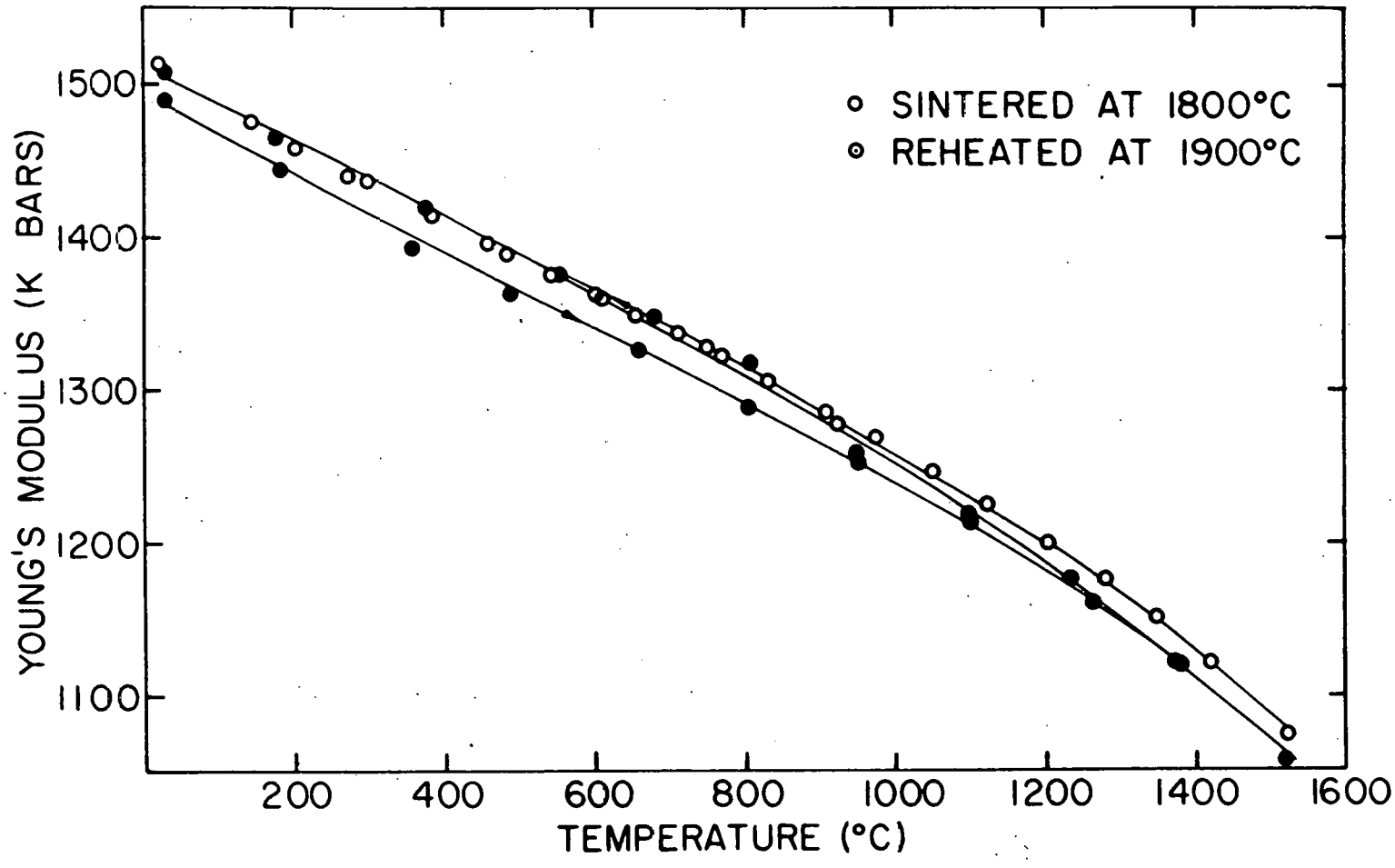

Figure 8. Elevated temperature Young's modulus (heating and cooling) of 94 mole % Eu_2O_3-6 mole % HfO_2

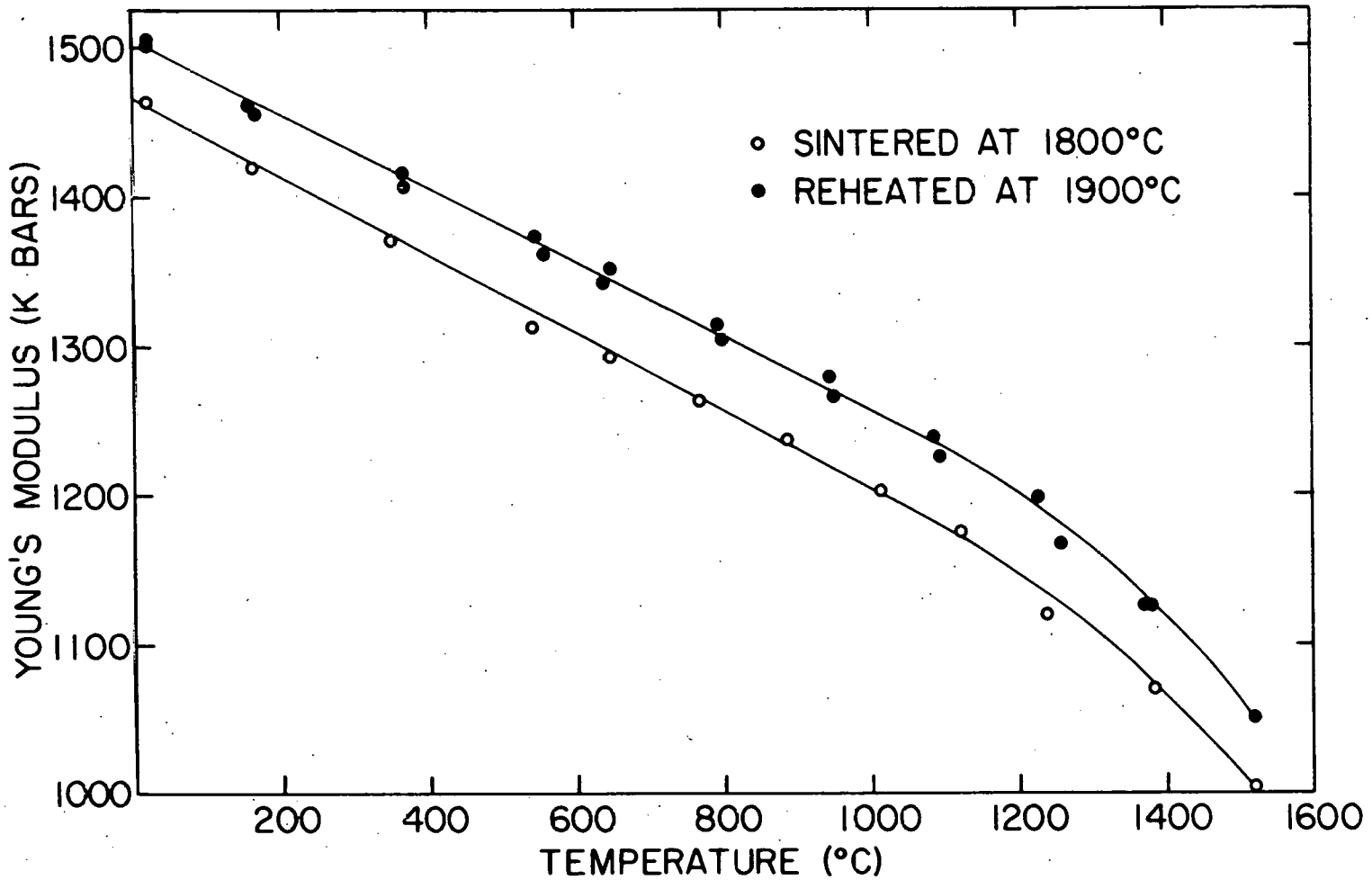

Figure 9. Elevated temperature Young's modulus (heating and cooling) of 92 mole % Eu_2O_3-8 mole % HfO_2

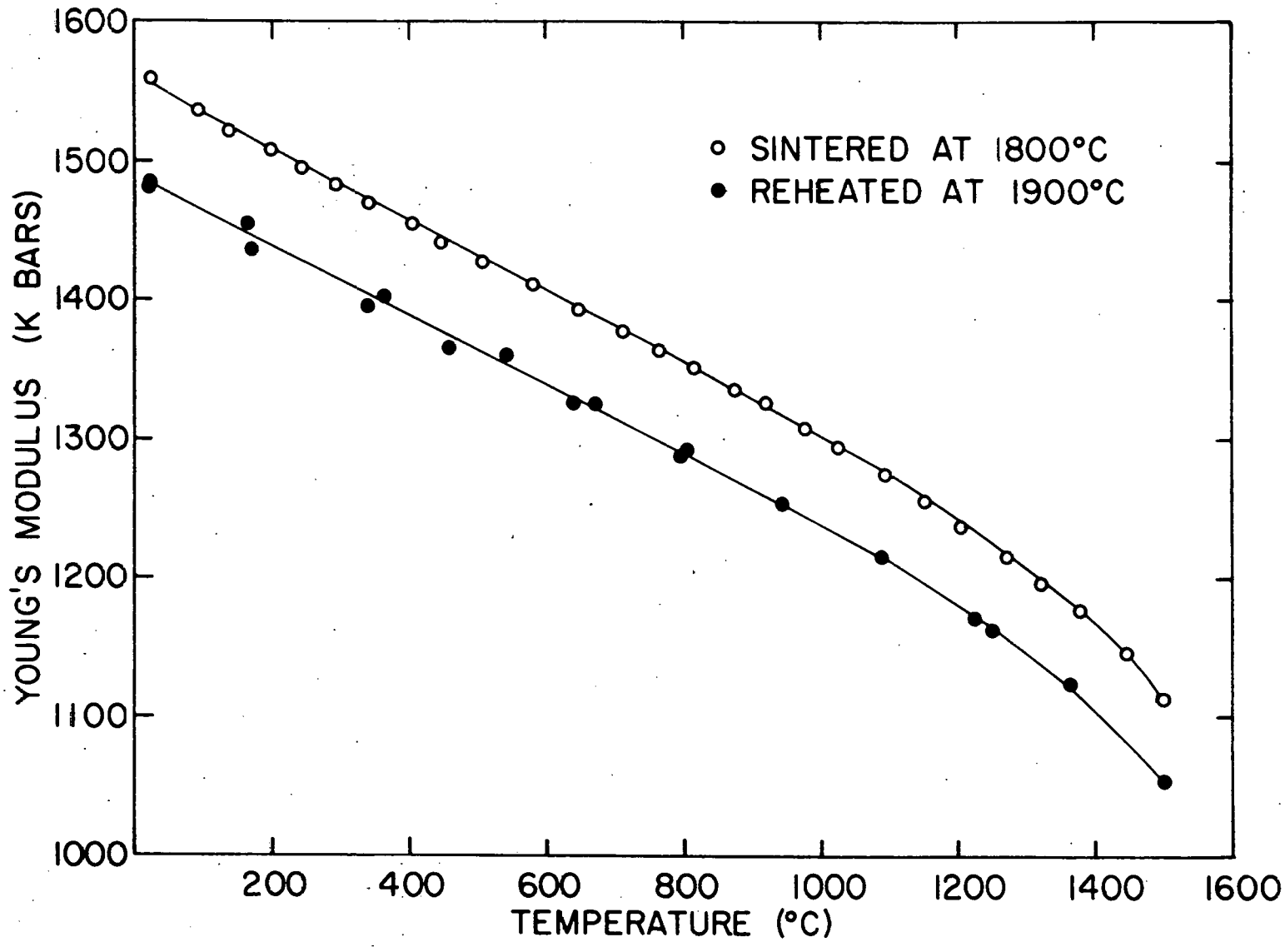

Figure 10. Elevated temperature Young's modulus (heating and cooling) of 90 mole % Eu_2O_3-10 mole % HfO_2

second heat treatment.

Very little is different in Fig. 6. Here, with a dopant level of 2 mole %, hysteresis is still seen after both firings. Again it appears that microcracking is more severe after the second firing step (bottom loop). The discrepancy in values at high temperature is a result of porosity variations within the specimen; the density was decreased by shaping and grinding after the second heat treatment.

Figure 7, 4 mole % HfO_2, displays the unusual behavior of Young's modulus which was found after the specimen had been refired to 1900°C. Before the second heat treatment (top loop), Young's modulus appeared to exhibit slightly less hysteresis than was found at lower additive concentrations for similar firing conditions. The very large hysteresis loop detected after the second firing (bottom loop) is not typical, however, of behavior at other compositions already discussed. In order to fully describe the behavior two heating segments are necessary in the plot. The lower heating curve shows elastic behavior of the specimen after it had been kept for several days at room temperature. Elasticity data obtained while heating and subsequently cooling of the specimen did not combine to form a closed loop, so a second heating segment was generated. This portion of the loop, the higher heating curve, was made immediately after the cooling section had been completed. This second heating curve did merge with the other

data points at high temperature and the second cooling curve (not shown) was similar to that of the first.

Room temperature elasticity measurements were made and recorded on this specimen for a period of time following the high temperature study. The modulus was found to decrease for several days until it stabilized at a value approximately equal to the initial value.

Only at this composition, 4 mole % HfO_2, and only after the 1900°C reheat treatment was such an aging effect seen. It is clear that microcracks did not form as rapidly during cooling of this specimen as they had in others already discussed. In this instance equilibrium and final stress release were gradually attained after a considerable time lapse. Microcracking was not eliminated by the addition of 4 mole % HfO_2 but it was significantly retarded.

Evidence of the actual elimination of microcracks is given by the 6 mole % HfO_2 specimen. These data are presented in Fig. 8. The specimen, after being sintered to 1800°C, showed none of the characteristics of internal cracking (top loop). A small hysteresis did develop following the 1900°C reheat treatment (bottom loop). Apparently a critical value in some structural parameter was exceeded during the 1900°C refire which allowed microcracks to develop.

In Fig. 9 no hysteresis was seen in either plot. For the preparation and firing conditions used in this study 8

mole % HfO_2 was sufficient to inhibit microcracking. If microcracks have not been totally eliminated, they are infrequent enough so that they do not affect elasticity performance.

This is confirmed by Fig. 10 in which the elastic behavior of 10 mole % HfO_2 doped Eu_2O_3 is displayed. At this composition both curves show linear temperature dependency.

Besides determining Young's modulus, this study also investigated shear modulus and Poisson's ratio. Information on shear modulus actually adds little new insight to either elastic behavior or microcracking. Figure 11 displays the shear modulus data obtained from several specimens. One specimen, a sintered pure Eu_2O_3 bar with 4.71% porosity, is the one for which Young's modulus was examined in Fig. 4. The shear modulus data reconfirms the existence of microcracks. Both telltale signs, the hysteresis loop and low room temperature value, are seen.

The hot pressed specimen is again included in this figure to show the similarity between Young's and shear moduli. Like the Young's modulus data graphed in Fig. 4, the shear data of Fig. 11 show the reversible linear behavior of a microcrack-free body.

Both of the specimens just described were sintered at 1800°C. The other curve in Fig. 11 gives shear data taken from the 6 mole % HfO_2 specimen following the secondary heat

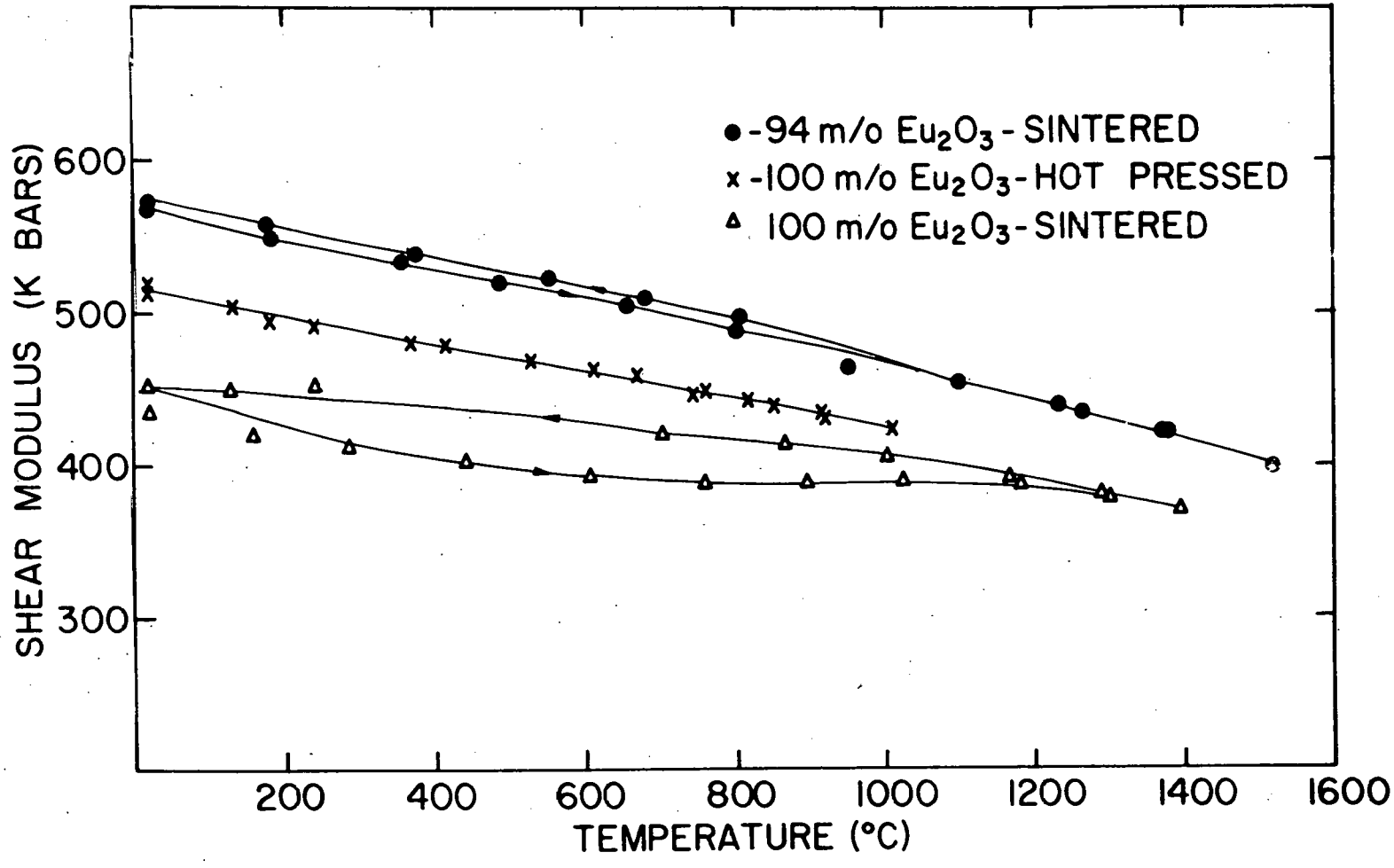

Figure 11. Elevated temperature shear modulus (heating and cooling) of three Eu_2O_3-HfO_2 specimens

treatment at 1900°C. A small hysteresis loop, again similar to the slight hysteresis reported in Fig. 8, is shown here. At every composition tested for both moduli, the behavior of Young's and shear moduli was similar.

Several of the specimens had small physical dimensions which produced unmeasurably high torsional frequencies and thus prohibited determination of shear modulus. In such cases it was also impossible to compute Poisson's ratio as both moduli are required in the calculation. Since Spinner et al. (41) concluded that a small (0.04) error in Poisson's ratio would not significantly affect the elasticity calculations, a constant value of 0.26, the value obtained from the hot pressed Eu_2O_3 specimen, was used when shear modulus was indeterminable.

Interestingly, whenever Poisson's ratio was available for microcracked specimens, it was found to be dependent on temperature. For example, Poisson's ratio for the sintered monoclinic pure europia specimen described in Figs. 4 and 11 varied from 0.25 at room temperature to 0.32 at 1400°C. Scatter in these data was such that curve fitting was not attempted. For specimens in which the moduli exhibited linear hysteresis-free behavior Poisson's ratio was found to be constant and consistent with values for other rare earth oxides (19,43).

Microstructural Analysis

The previous section has established that the microcracking seen in pure monoclinic Eu_2O_3 can be overcome by the addition of a sufficient quantity of HfO_2. Certainly some structural property or properties must have been altered by the presence of HfO_2. To determine any structural changes X-ray diffraction and microscopic studies were made on each specimen.

An X-ray diffraction study revealed that at low concentrations HfO_2 went into solid solution in the monoclinic Eu_2O_3 but at higher concentrations formed a separate cubic phase. Figure 12, which summarizes this study, is not meant to be construed as a partial phase study but only to graphically display the phases present at room temperature after sintering or refiring at the temperature indicated.

The monoclinic form of pure sintered Eu_2O_3, identified by the diffraction pattern given by Glushkova and Boganov (16), remained quite stable at room temperature. An X-ray diffraction pattern taken nearly a year after sintering revealed only a faint cubic pattern.

The exact structure of the cubic phase could not be determined from the X-ray diffraction patterns developed during this study. It is possible that it is fluorite structured since Radzewitz (14) has identified a two phase region, fluorite (cubic) and B-type rare earth oxide (monoclinic),

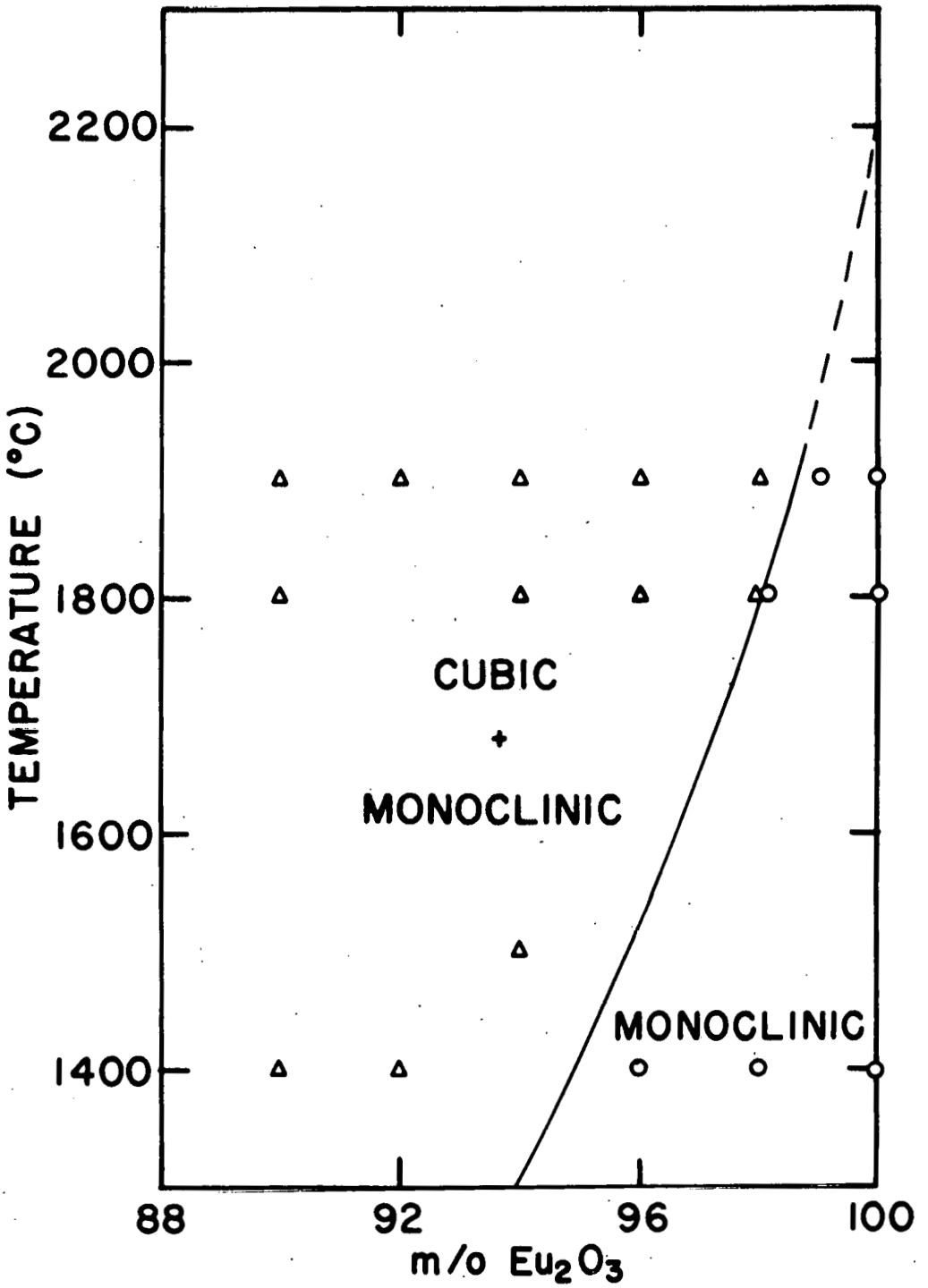

Figure 12. Phases present after sintering or reheating of some Eu_2O_3-HfO_2 compositions

at the composition 82 mole % Eu_2O_3-18 mole % HfO_2 at 1500°C. A more recent study[1] suggests that the cubic form seen in this study is actually the rare earth oxide C-type (cubic) europia structure. Such an identification would be consistent with the structures found by Spiridinov et al. (51) in their investigation of a similar system, HfO_2-Gd_2O_3.

The information provided on phase stability with respect to sintering at 1400°C is included because it supports the reliability of the other data. In addition, it shows that a single phase cubic europia form cannot be produced by the addition of up to 10 mole % HfO_2. This temperature, 1400°C, was chosen as being a minimum temperature for acceptable sintering. The X-ray information indicates then that such a phase, which would possess isotropic thermal expansion, cannot be produced by sintering in the compositional region of interest.

Photomicrographs of the specimens, taken both before and after they were refired at 1900°C, are presented in Figs. 13-18. The same magnification (161X) was used on each photo to show the relative grain size.

Pure Eu_2O_3, Fig. 13, sinters to form extremely large grained specimens. An average grain size of 117 μm before the reheat treatment is enlarged to 153 μm after this second firing. These values are in the range reported by Ploetz et

[1]R. W. Scheidecker. Ames Laboratory, ERDA, Iowa State University, Ames, Iowa. Private communication. May 14, 1975.

Figure 13a. Photomicrograph of a polished section of a 0 mole % HfO_2 (100 mole % Eu_2O_3) specimen after sintering at 1800°C. Arrow indicates unusual cracking.

Figure 13b. Photomicrograph of a polished section of a 0 mole % HfO_2 (100 mole % Eu_2O_3) specimen after reheating at 1900°C.

THIS PAGE

WAS INTENTIONALLY

LEFT BLANK

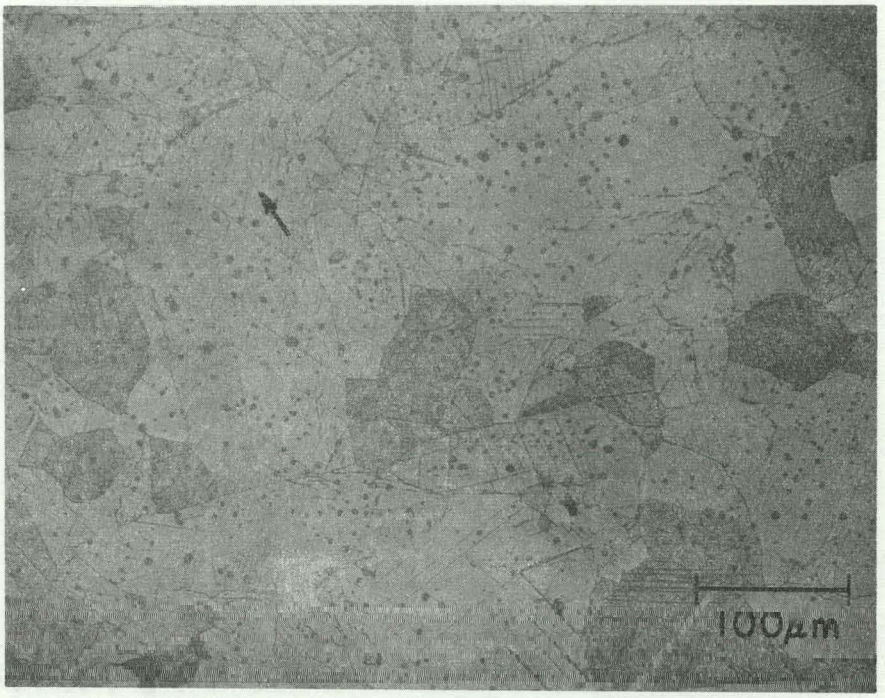
100μm

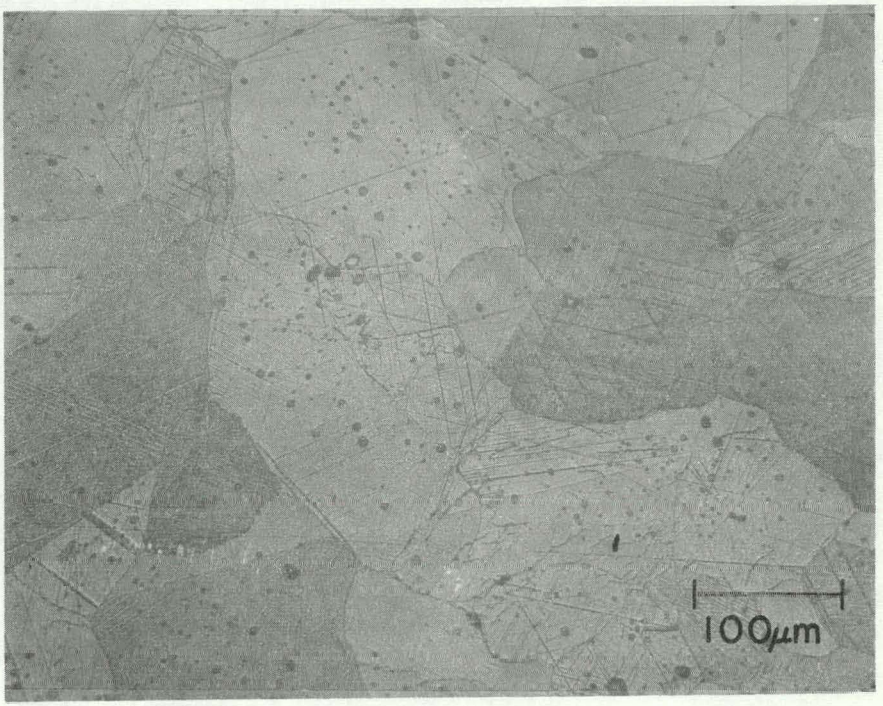
100μm

Figure 13c. Scanning electron micrograph of a polished section of a 0 mole % HfO_2 (100 mole % Eu_2O_3) specimen after sintering at 1800°C.

Figure 13d. Photomicrograph of a polished section of hot-pressed pure Eu_2O_3.

THIS PAGE
WAS INTENTIONALLY
LEFT BLANK

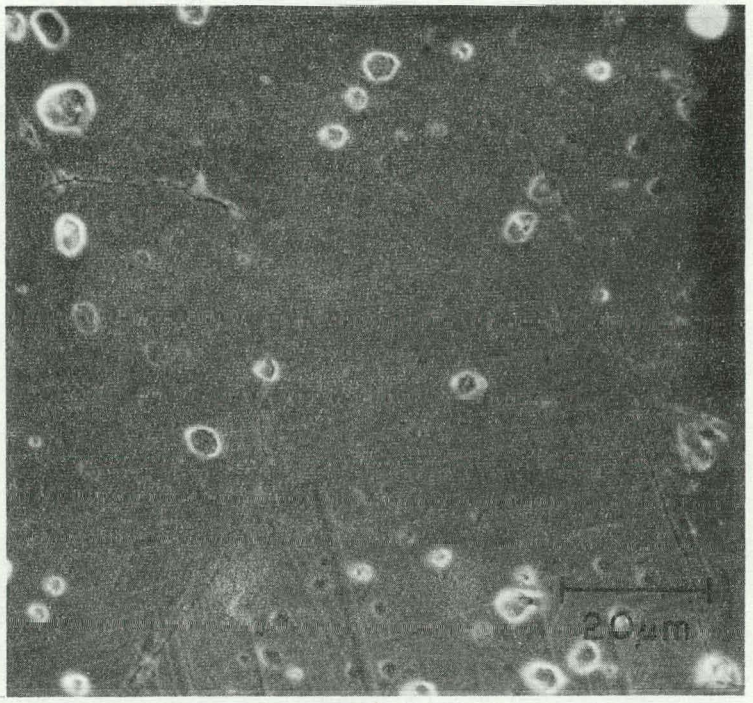
20μm

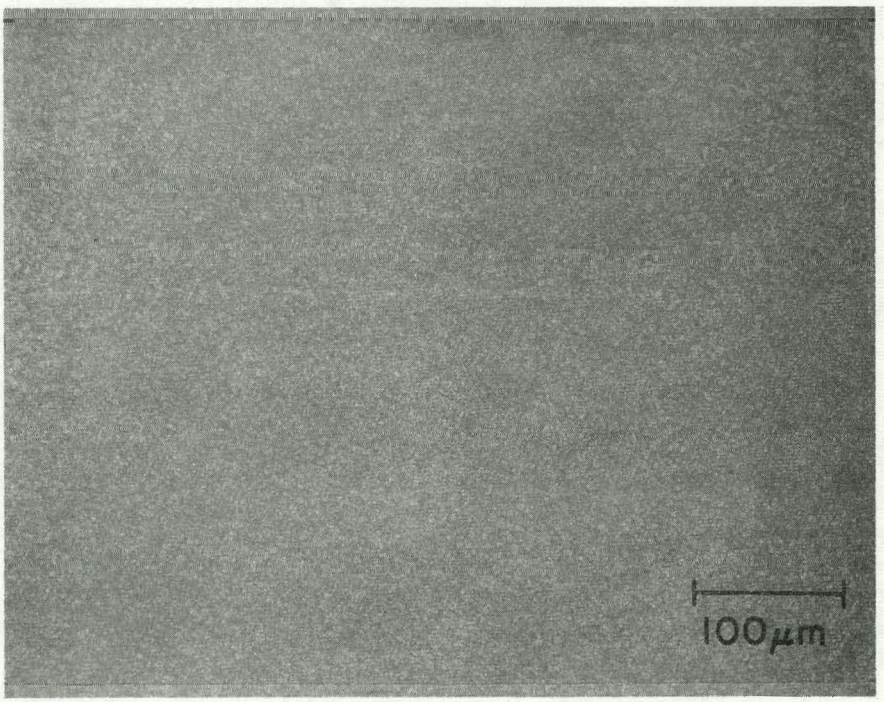
100μm

al. (2). Their specimens, which were also held at the sintering temperature of 1800°C for one hour, were found to have grains in the range of 180-360 μm. Ploetz et al. (2) also found the same twinning features as are evident in the photos of Fig. 13a and 13b. More importantly their micrograph shows unusual cracking much like that seen in Fig. 13a. In their report no mention was made of this cracking although the photomicrographs they presented of the other monoclinic rare earth sesquioxides displayed no such features.

In the hope that these cracks were actually the infrequently observed but much discussed microcracks, a scanning electron microscope photo was made of the polished section. This photo is reproduced in Fig. 13c. After an examination of both types of photos certain features become apparent. The short but rather consistent length of these cracks, their jagged appearance, the concentration of these cracks in some grains and the total absence of them in others, and the observation that none of them cross grain boundaries all support the hypothesis that they are anisotropically induced microcracks. Scanning electron photomicrographs, when viewed stereoscopically, show these cracks to be quite distinct from and deeper than other surface features. Of course it can not be conclusively stated that these cracks were not produced during either the grinding, mounting, or polishing operations.

Much smaller grains (5-6 μm) were found in the hot

pressed pure Eu_2O_3 specimen as would be anticipated. A photomicrograph of the structure of this specimen is shown in Fig. 13d. Grains are so small that neither twinning nor microcracking can be observed.

The next four figures, Figs. 14-17, show that the grain size decreases monotomically as larger concentrations of HfO_2 are added. Photomicrographs of the 10 mole % HfO_2 specimen which are given in Fig. 18 show a reversal in the trend toward smaller sized grains. This composition is the only one in which two phases are clearly evident. The micrograph taken after the specimen was refired to 1900°C shows isolated pockets of one phase produced as grains of the second phase coarsened around them. Positive identification of the larger grains as either monoclinic or fluorite structure was not attempted.

The grain size information obtained from all the specimens is combined and presented in Fig. 19. Where possible the average grain size of both specimens of each composition is displayed. This figure very clearly shows the trend of grain growth suppression as HfO_2 is added to Eu_2O_3.

The series of photos just presented also shows that the porosity of a specimen changes with composition and grain size. Since phase diagram and other information is not available absolute densities and porosities cannot be calculated. However the grain size and density information tabulated in

Figure 14a. Photomicrograph of a polished section of a 2 mole % HfO_2 (98 mole % Eu_2O_3) specimen after sintering at 1800°C.

Figure 14b. Photomicrograph of a polished section of a 2 mole % HfO_2 (98 mole % Eu_2O_3) specimen after reheating at 1900°C.

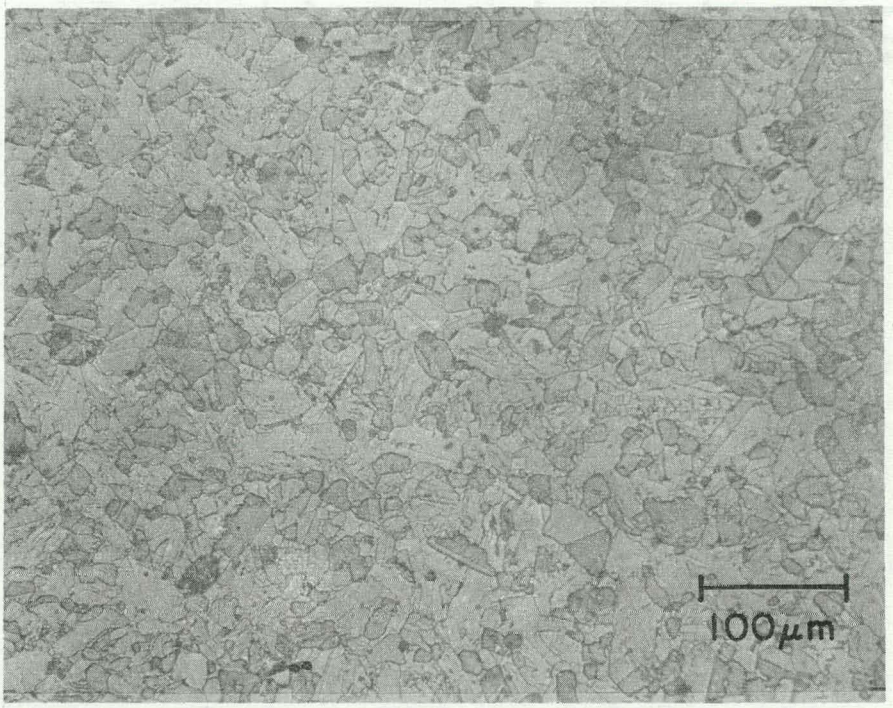
100μm

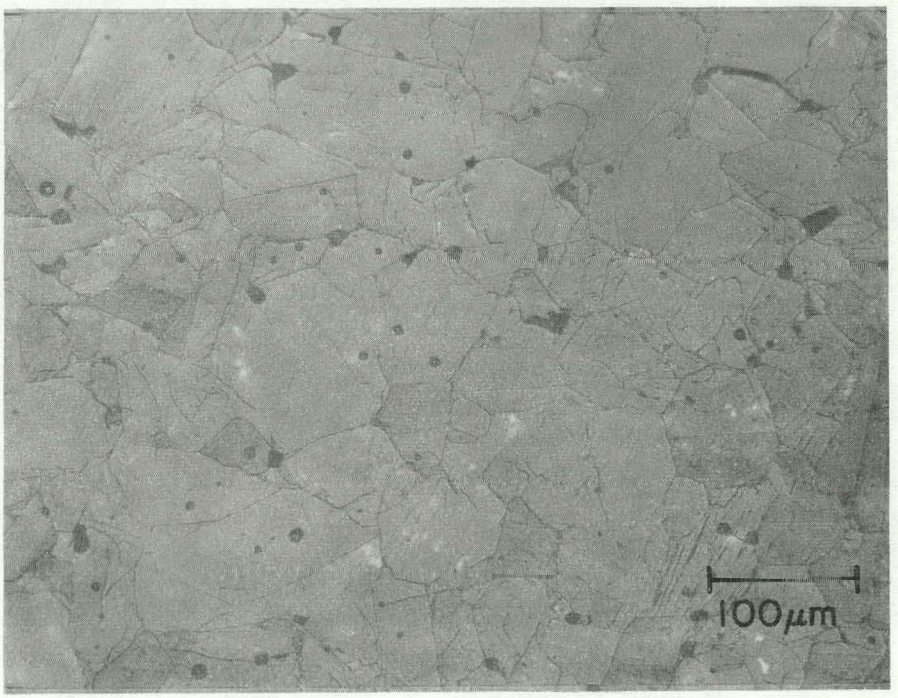
100μm

Figure 15a. Photomicrograph of a polished section of a 4 mole % HfO_2 (96 mole % Eu_2O_3) specimen after sintering at 1800°C.

Figure 15b. Photomicrograph of a polished section of a 4 mole % HfO_2 (96 mole % Eu_2O_3) specimen after reheating at 1900°C.

THIS PAGE
WAS INTENTIONALLY
LEFT BLANK

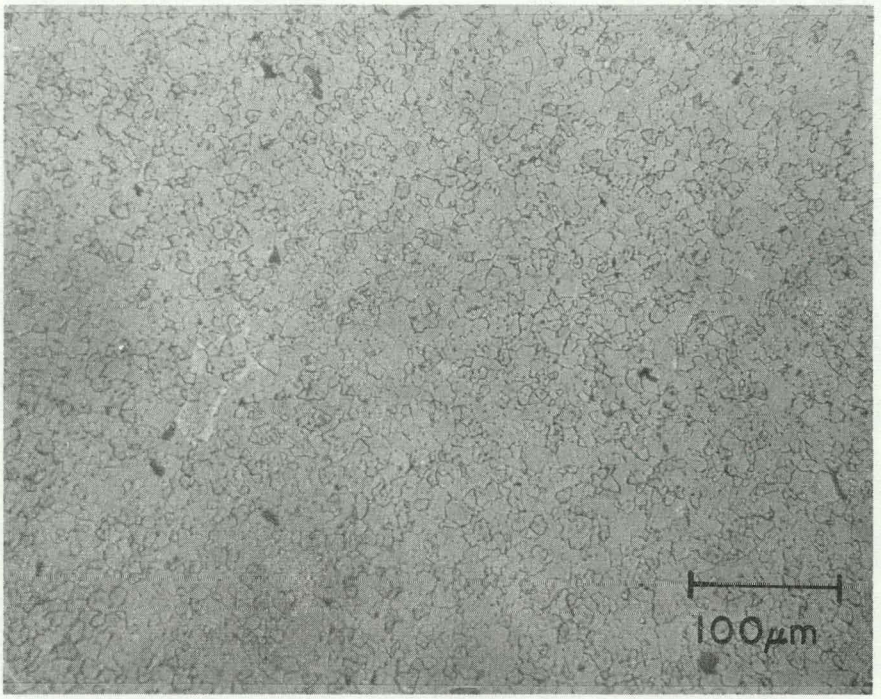
100μm

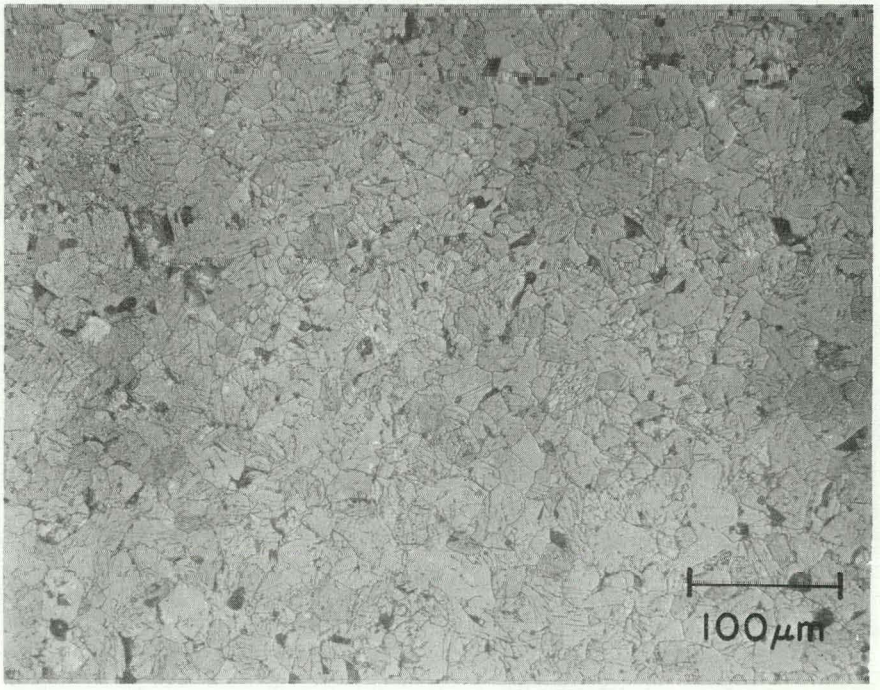
100μm

Figure 16a. Photomicrograph of a polished section of a 6 mole % HfO_2 (94 mole % Eu_2O_3) specimen after sintering at 1800°C.

Figure 16b. Photomicrograph of a polished section of a 6 mole % HfO_2 (94 mole % Eu_2O_3) specimen after reheating at 1900°C.

THIS PAGE
WAS INTENTIONALLY
LEFT BLANK

Figure 16a. Photomicrograph of a polished section of a 6 mole % HfO_2 (94 mole % Eu_2O_3) specimen after sintering at 1800°C.

Figure 16b. Photomicrograph of a polished section of a 6 mole % HfO_2 (94 mole % Eu_2O_3) specimen after reheating at 1900°C.

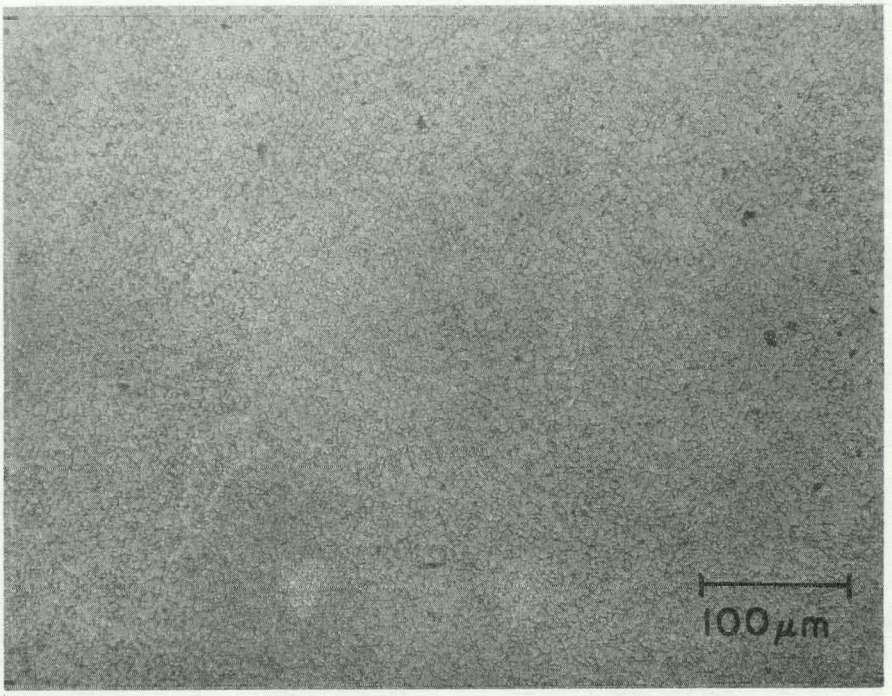
100 μm

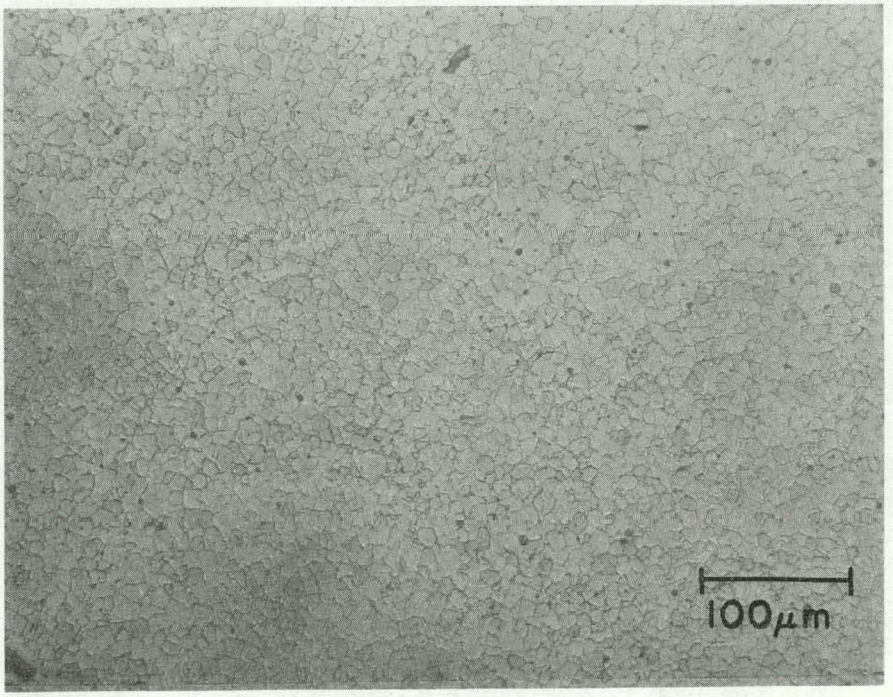
100μm

Figure 17. Photomicrograph of a polished section of an 8 mole % HfO_2 (92 mole % Eu_2O_3) specimen after reheating at 1900°C.

THIS PAGE
WAS INTENTIONALLY
LEFT BLANK

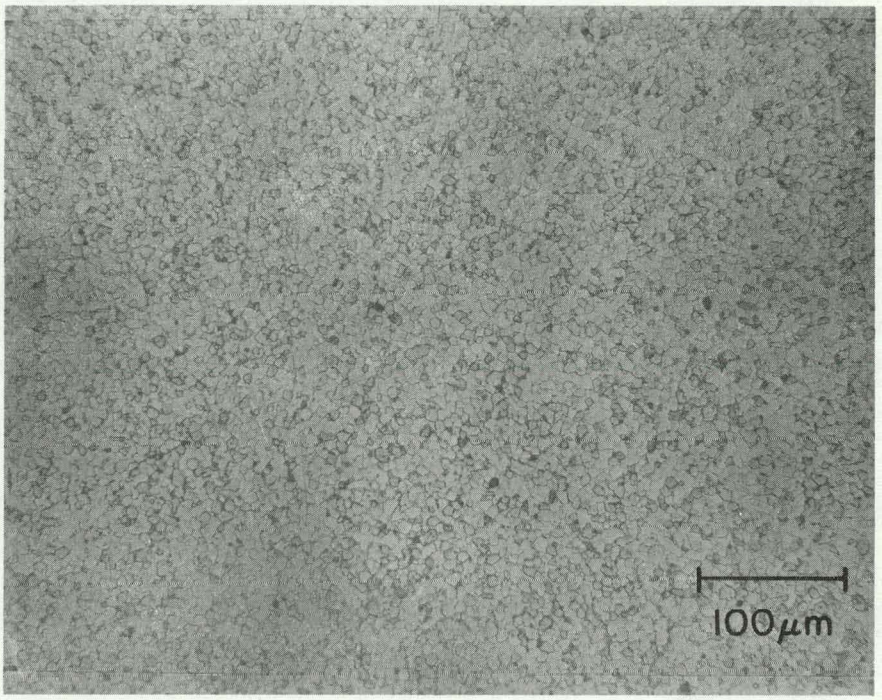
100μm

Figure 18a. Photomicrograph of a polished section of a 10 mole % HfO_2 (90 mole % Eu_2O_3) specimen after sintering at 1800°C.

Figure 18b. Photomicrograph of a polished section of a 10 mole % HfO_2 (90 mole % Eu_2O_3) specimen after reheating at 1900°C.

THIS PAGE
WAS INTENTIONALLY
LEFT BLANK

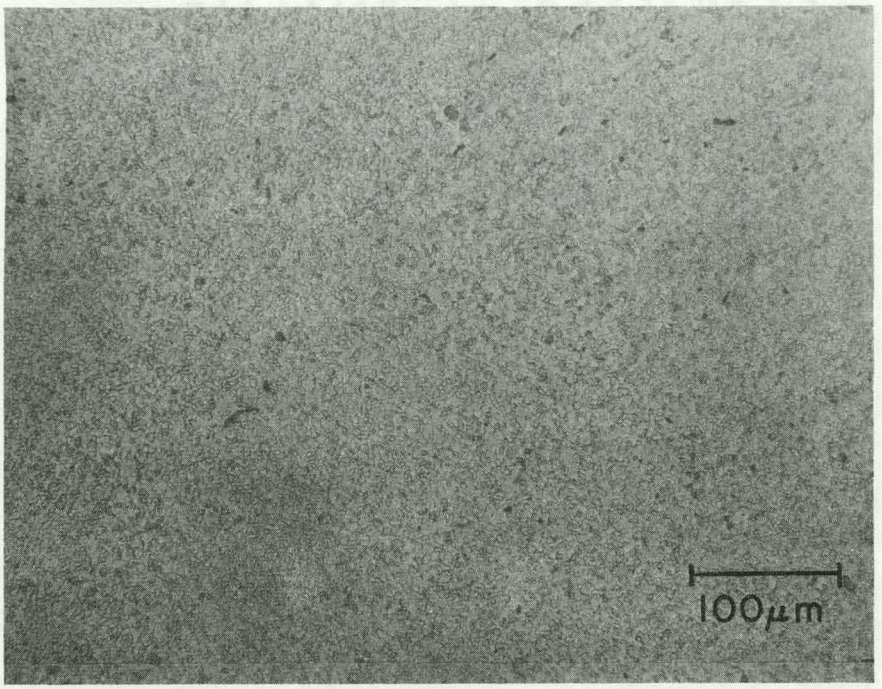
100μm

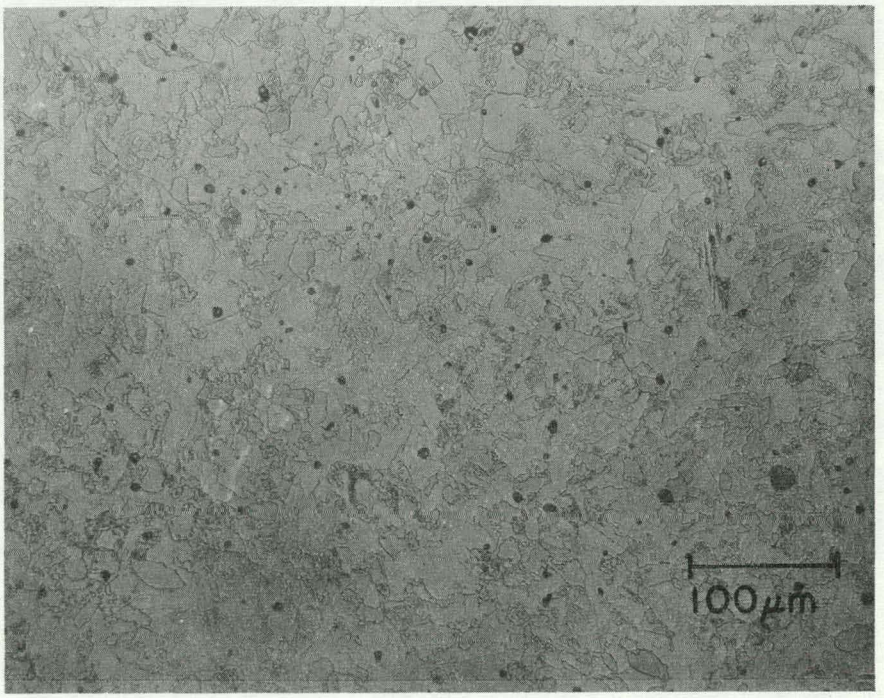
100μm

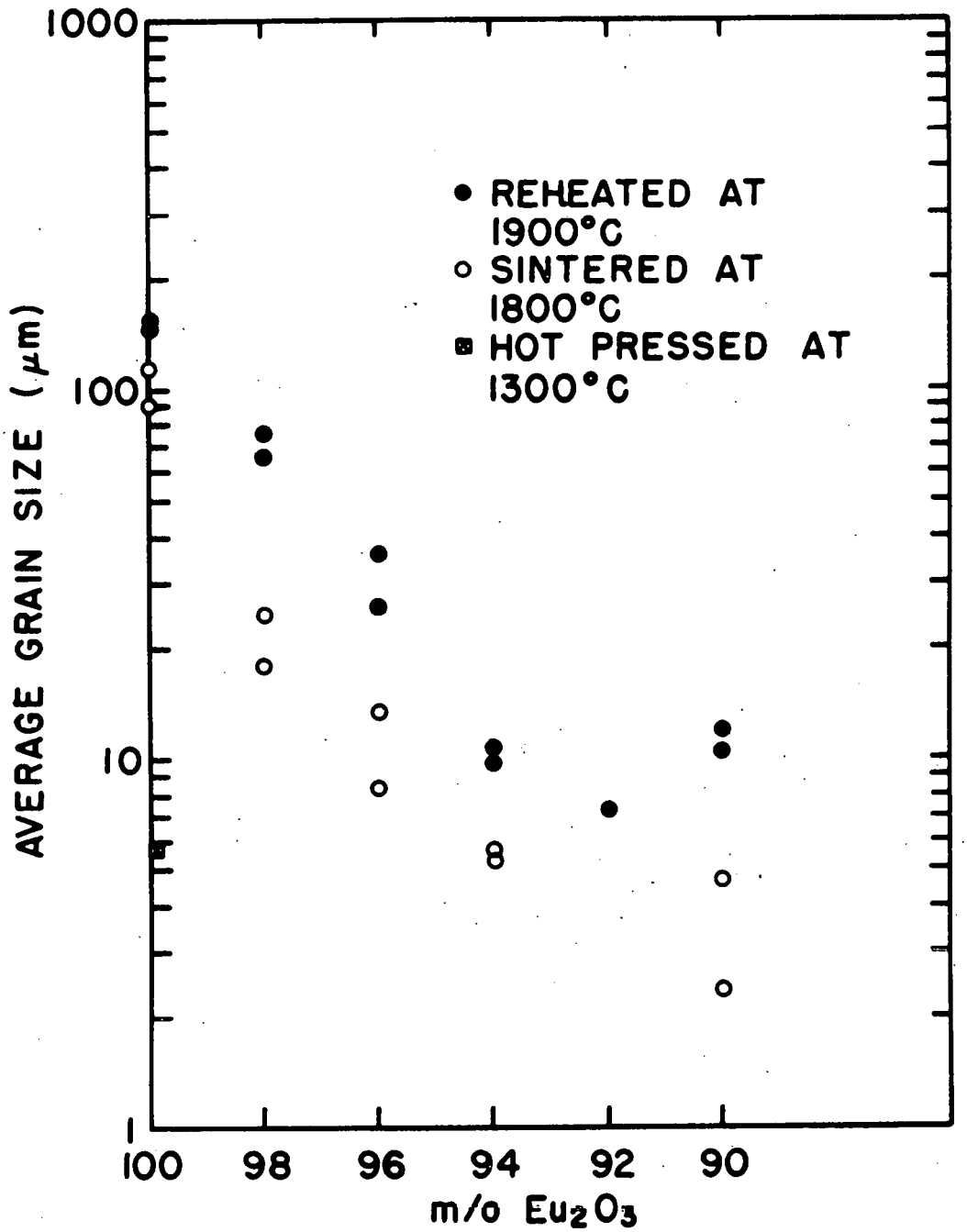

Figure 19. Average grain size of specimens of various Eu_2O_3-HfO_2 compositions

Appendix B shows the trend. For example, pure Eu_2O_3 was sintered to an average density of 7.6 gm/cm^3 while using the same conditions compositions with only 4 mole % to 8 mole % HfO_2 were sintered to densities in excess of 7.9 gm/cm^3.

Additional Testing

Measurements of thermal expansion were made at each composition of interest. Results of the expansion runs are detailed in Appendix C. Values listed in Table 3 show only the mean coefficients of expansion.

Table 3. Mean coefficients of expansion from 25°C to 1150°C for six Eu_2O_3-HfO_2 compositions

Composition (mole % HfO_2)	x10^6(°C^{-1})
0	9.9
2	10.2
4	10.2
6	10.4
8	10.3
10	10.2

Other investigators have determined similar thermal expansion coefficients for sintered monoclinic Eu_2O_3. Curtis and Tharp (4) found a value of 10.30x10^{-6} °C^{-1} over a range of 0°C-1200°C. Wilfong et al. (52) reported 10.35x10^{-6} °C^{-1} from 25°C to 1000°C. Still another report, by Ploetz et al. (2) listed an expansion coefficient of 10.5x10^{-6} °C^{-1} over the interval from 30°C to 840°C.

These published values agree fairly well with the coeffi-

cients determined in this study. Over the small compositional range investigated here, a large change in expansion rates would not be expected. The somewhat lower value obtained from pure Eu_2O_3 in this study may be real or only a statistical variation. The results of this study prove only that the lengths of all specimens increase monotonically with temperature. A visual analysis of plotted thermal expansion data ($\Delta\ell/\ell_o$ versus temperature) found the slopes for all compositions to be consistent. However if the coefficient of pure Eu_2O_3 is significantly different from that of the doped specimens, the difference could easily be explained from a crack healing approach. Microcracks, which were found to exist in this particular specimen at low temperature, heal as the temperature is increased. Such crack healing would naturally reduce the net expansion of the specimen. Manning et al. (53) and Kuszyk and Bradt (32) found such healing to appreciably affect thermal expansion behavior.

Exposure of specimens to boiling water provided no real quantitative measurement of their stability. The condition of the materials was observed during testing and the amount of time required for complete loss of integrity and formation of substantial powder was reported. There did appear to be a correlation between grain size and attack rate although none of the specimens displayed extremely good attack resistance. Sintered pure Eu_2O_3 specimens broke apart after only one hour

in boiling water. Europia specimens doped with 2 mole %, 4 mole %, and 6 mole % HfO_2 all crumbled after 2 to 2 1/2 hours. After 3 hours of attack the specimens containing 10 mole % HfO_2 also failed. Of the sintered compositions that containing 8 mole % HfO_2 performed best; it lasted for over 5 hours. Superior in performance to all of the sintered specimens, however, was the hot pressed Eu_2O_3 material. Approximately 8 hours elapsed before it degraded to a similar condition.

Without establishing the exact relation between structure and resistance to boiling water attack, it is clear that reduction of grain size, produced either by doping or hot pressing, improved the resistance of monoclinic Eu_2O_3.

An observation on the stoichiometry of various compositions was also made. After high temperature elasticity measurements were made on the prisms within the vacuum chamber, specimens of each composition containing HfO_2 were blackish in color. The pure europia specimens, however, retained their characteristic tannish-pink color. Apparently the addition of some HfO_2 caused the europia to be even more susceptible to reduction. With the atmosphere extremes ($<1x10^{-5}$ torr at 1500°C) used in this study, such reduction was minimal. Weight measurements before and after high temperature elasticity studies revealed that the largest weight change, less than 0.015%, occurred in a 10 mole % specimen. At each composition, the color of the specimens reverted to the original

light tan after heating in air to 900°C. Elastic behavior of the specimens was not significantly affected by such reduction and reoxidation.

Control of Microstructure and Microcracking

From the experimental results already described it is clear that the addition of small percentages of HfO_2 has significantly altered some of the properties of Eu_2O_3. While the thermal expansion coefficients remained relatively constant, both elastic behavior and microstructure were modified. This suggests that there may be a relationship between composition, grain size, and elasticity. The effect on the elastic properties is directly attributable to microcracking so the relationship to be developed is between composition, grain size, and microcracking.

The effect of composition on grain size is most obvious. In this experiment, grain growth was suppressed to a degree proportional to the amount of HfO_2 added. Suppression of grain growth by the addition of minor amounts of second phase is a widely used procedure in the fabrication of ceramics. Even at 2 mole % HfO_2 where a second phase was not detected inhomogeneity within the solid solution would inhibit grain growth.

At each of the compositions analyzed, regardless of whether a second phase was introduced, a monoclinic Eu_2O_3 phase was detected. Because of the thermal expansion aniso-

tropy inherent in the monoclinic structure, microstresses must have developed within each specimen at each composition.

The essence of the problem then is to explain the relationship of grain size and microcracking. This is exactly the question discussed by Kuszyk and Bradt (32). Their concept of a critical grain size for microcracking should also be applicable in this study.

In this study evidence of microcracking was discovered at four compositions. They were seen both before and after the secondary heat treatment in sintered specimens containing 0 mole %, 2 mole %, and 4 mole % HfO_2. After being refired to 1900°C specimens of the composition 6 mole % HfO_2 also displayed the traits. Evidence of microcracking was not found at 6 mole % HfO_2 prior to the reheat nor was it ever observed at 8 mole % or 10 mole % HfO_2. In addition no indications of microcracking were found during testing of the hot pressed pure europia specimen.

It can be seen by reviewing Fig. 19, the plot of grain size versus composition, that microcracking was evident only in specimens which had an average grain size larger than 8 microns. Whenever the grain size was kept below 8 microns, neither Young's nor shear moduli suggested abnormal behavior. For the only exception to this limit, at 10 mole % HfO_2, the grains were not positively identified. The larger grains of this specimen may have had an isotropic cubic structure rather than an anisotropic monoclinic structure.

CONCLUSIONS

1) Monoclinic Eu_2O_3 has a strong tendency toward grain growth during sintering. When it is cooled from the sintering temperature the large grained sintered Eu_2O_3 undergoes extensive microcracking.
2) Small grain sized hot pressed monoclinic Eu_2O_3 does not develop sufficient stresses to form microcracks as it is cooled from the the hot pressing temperature.
3) The addition of small concentrations of HfO_2 to Eu_2O_3 suppresses grain growth during sintering. Hafnia also acts as an aid in sintering, reducing the residual porosity. This decrease in porosity offsets some of the loss in nuclear worth caused by the substitution of hafnium for europium.
4) Sufficiently small sized anisotropic grains in a specimen prohibit the development of strain energies necessary for microcracking. A critical grain size of approximately 8 μm is necessary to produce microcracking in monoclinic Eu_2O_3.
5) Microcracked specimens possess unusual elastic behavior. Both Young's and shear moduli of such specimens have abnormally low room temperature values and display a hysteresis between heating and cooling values.
6) Hot pressed Eu_2O_3 and sintered compositions without microcracks show normal elastic behavior.

7) Young's and shear moduli of theoretically dense micro-crack free monoclinic Eu_2O_3 are projected to be 1477 Kbars and 584 Kbars, respectively.

8) Thermal expansion coefficients in the range of 9.9 to 10.4×10^{-6} $°C^{-1}$ are not significantly affected by compositional changes over the range of this study.

9) Even through the use of sintering temperatures as low as 1400°C, a single phase cubic structure cannot be formed by the addition to Eu_2O_3 of up to 10 mole % HfO_2.

LITERATURE CITED

1. Gray, W. J. 1973. A preliminary survey of potential fast reactor control materials. Battelle Pacific Northwest Laboratories BNWL-B-297.

2. Ploetz, G. L., C. W. Krystyniak, and H. E. Dumas. 1958. Sintering characteristics of rare-earth oxides. J. Amer. Ceram. Soc. 41(12):551-554.

3. Leitten, C. F., Jr., and R. J. Beaver. 1968. Use of lanthanide oxide neutron absorbers in pressurized water reactors. Nuc. Appl. 4:399-417.

4. Curtis, C. E., and A. G. Tharp. 1959. Ceramic properties of europium oxide. J. Amer. Ceram. Soc. 42(3):151-156.

5. Pashos, T. J. 1968. Materials for control of water cooled power reactors. Nuc. Appl. 4:395-398.

6. Ploetz, G. L. 1960. Ceramic materials for nuclear reactor controls and poison. Amer. Ceram. Soc. Bull. 39(7):362-365.

7. Ray, W. E. 1963. Fabrication of control rods for nuclear reactors. An AEC monograph. Rowman and Littlefield, New York. 229 pp.

8. Spink, D. R., and J. H. Schemel. 1973. The development of rare-earth pyrohafnates for power reactor control-rod materials. J. Nuc. Mat. 49(73074):1-9.

9. Lynch, C. T. 1970. Hafnium oxide. Pages 193-216 in A. M. Alper, ed. High Temperature Oxides. Part II: Oxides of Rare Earths, Titanium, Zirconium, Hafnium, Niobium, and Tantalum. Academic Press, New York.

10. Tuttle, R. J., and T. H. Springer. 1972. Reactivity worths of boron, tantalum, and europium in a fast reactor spectrum. Nuc. Science and Eng. 49:468-481.

11. Goldman, K. M., and T. Walker. 1962. Properties of hafnium. Pages 153-161 in W. K. Anderson and J. S. Theilacker, eds. Neutron Absorber Materials for Reactor Control. Naval Reactors, Division of Reactor Development, USAEC, Washington, D.C.

12. McMasters, O. D., and K. A. Gschneidner. 1964. Rare earth intermetallic compounds. Pages 93-158 in J. T. Waber, P. Chiotti and W. N. Miner, eds. Nuclear Metallurgy, Vol. X. Compounds of Interest in Nuclear Reactor Technology. Edwards Brothers, Inc., Ann Arbor, Mich.

13. Spenke, H. 1972. Suitability of europium as absorbing material in fast reactors. Atomwirt. Atomtech. 17(3): 161-164.

14. Radzewitz, H. 1966. Festkoerperchemische untersuchungen ueber die systeme $SeO_{1.5}$-ZrO_2(HfO_2), $AmO_{1.5}$-ZrO_2(HfO_2-ThO_2)-O_2, and TiO_2-NpO_2(PuO_2). Institut fuer Radiochemie, Karlsruhe. 53 pp.

15. Warshaw, I., and R. Roy. 1961. Polymorphism of the rare earth sesquioxides. J. Phys. Chem. 65:2048-2051.

16. Glushkova, V. B., and A. G. Boganov. 1965. Izvestiya Akademii Nauk SSSR, Seriya Khimicheskaya 7:1131-1138.

17. Hoekstra, H. R. 1966. Phase relationships in the rare earth sesquioxides at high pressure. Inorg. Chem. 5(5): 754-757.

18. Hunter, O., Jr., H. J. Korklan, and R. R. Suchomel. 1974. Elastic properties of polycrystalline monoclinic Sm_2O_3. J. Amer. Ceram. Soc. 57(6):267-268.

19. Haglund, J. A., and O. Hunter, Jr. 1973. Elastic properties of polycrystalline monoclinic Gd_2O_3. J. Amer. Ceram. Soc. 56(6):327-329.

20. McCarthy, G. J. 1974. Oxygen fugacity-temperature diagram for the Eu-O system. J. Amer. Ceram. Soc. 57(11): 502.

21. Pasto, A. E., M. M. Martin, and R. G. Donnelly. 1974. Vacuum sintering and hot pressing of Eu_2O_3. Pages 14-22 in CONF-741002-P1, 11th Rare Earth Research Conference, Traverse City, Michigan.

22. Patriarca, P. 1974. Fuels and Materials Development Program. Quarterly Progress Report for period ending December 31, 1973. Oak Ridge National Laboratory ORNL-TM-4524.

23. Wachtman, J. B., Jr. 1967. Mechanical properties of ceramics: an introductory survey. Amer. Ceram. Soc. Bull. 46(8):756-774.

24. Buessem, W. R. 1961. Internal ruptures and recombinations in anisotropic ceramic materials. Pages 127-148 in W. W. Kriegel and H. Palmour, eds. Mechanical Properties of Engineering Ceramics. Interscience Publishers, New York.

25. Likhachev, V. A. 1961. Microstructural strains due to thermal anisotropy. Soviet Physics-Solid State 3(6): 1330-1336.

26. Ault, N. N., and H. F. G. Ueltz. 1953. Sonic analysis for solid bodies. J. Amer. Ceram. Soc. 36(6):199-203.

27. Hunter, O., Jr., and W. E. Brownell. 1967. Thermal expansion and elastic properties of two-phase ceramic bodies. J. Amer. Ceram. Soc. 50(1):19-22.

28. Manning, W. R., and O. Hunter, Jr. 1973. Anomalous elastic behavior of polycrystalline Nb_2O_5. J. Amer. Ceram. Soc. 56(11):602-603.

29. Bush, E. A., and F. A. Hummel. 1959. High-temperature mechanical properties of ceramic materials: II. Beta-eucryptite. J. Amer. Ceram. Soc. 42(8):388-391.

30. Matsuo, Y., and H. Sasaki. 1966. Effect of Grain Size on microcracking in lead titanate ceramics. J. Amer.

31. Bush, E. A., and F. A. Hummel. 1958. High-temperature mechanical properties of ceramic materials: I. Magnesium dititanate. J. Amer. Ceram. Soc. 41(6):189-195.

32. Kuszyk, J. A., and R. C. Bradt. 1973. Influence of grain size on effects of thermal expansion anisotropy in $MgTi_2O_5$. J. Amer. Ceram. Soc. 56(8):420-423.

33. Hasselman, D. P. H. 1963. Elastic energy at fracture and surface energy as design criteria for thermal shock. J. Amer. Ceram. Soc. 46(11):535-540.

34. McNees, R. A., and R. A. Potter. 1962. Europium oxide studies. Pages 16-22 in L. D. Schaffer, Coordinator. Army Reactors Program Progress Report, Jan. 31. Oak Ridge National Laboratory ORNL-3231.

35. Fullman, R. L. 1953. Measurement of particle sizes in opaque bodies. Jour. Metal. Trans. AIME 1953:447-452.

36. Forster, F. 1937. A new method for the determination of the modulus of elasticity and damping. Zeit. Metallkunde 29(4):109-115.

37. Spinner, S., and W. E. Tefft. 1961. A method for determining mechanical resonance frequencies and for calculating elastic moduli from these frequencies. A.S.T.M. Proc. 61:1221-1238.

38. Manning, W. R. 1970. Anomalous elastic behavior of polycrystalline Nb_2O_5. Unpublished Ph.D. thesis. Ames, Iowa, Library, Iowa State University of Science and Technology. 150 pp.

39. Pickett, G. 1945. Equations for computing elastic constants from flexural and torsional resonant frequencies of vibration of prisms and cylinders. A.S.T.M. Proc. 45: 846-865.

40. Hasselman, D. P. H. 1961. Tables for the computation of shear modulus and Young's modulus of elasticity from resonant frequencies of rectangular prisms. Carborundum Co., Niagara Falls, New York.

41. Spinner, S., T. W. Reichard, and W. E. Tefft. 1960. A comparison of experimental and theoretical relations between Young's modulus and the flexural and longitudinal resonance frequencies of uniform bars. J. Res. Nat. Bur. Stand. 64A(2):147-155.

42. Marlowe, M. O., and D. R. Wilder. 1965. Elasticity and internal friction of polycrystalline yttrium oxide. J. Amer. Ceram. Soc. 48(5):227-233.

43. Manning, W. R., and O. Hunter, Jr. 1969. Elastic properties of polycrystalline yttrium oxide, holmium oxide, and erbium oxide: High-temperature measurements. J. Amer. Ceram. Soc. 52(9):492-496.

44. Spriggs, R. M. 1961. Expression for effect of porosity on elastic modulus of polycrystalline refractory materials, particularly aluminum oxide. J. Amer. Ceram. Soc. 44(12):628-629.

45. Hasselman, D. P. H. 1962. On the porosity dependence of the elastic moduli of polycrystalline refractory materials. J. Amer. Ceram. Soc. 45(9):452-453.

46. Wachtman, J. B., Jr., and D. G. Lam, Jr. 1959. Young's modulus of various refractory materials as a function ot temperature. J. Amer. Ceram. Soc. 42(5):254-260.

47. Schwartz, B. 1952. Thermal stress failure of pure refractory oxides. J. Amer. Ceram. Soc. 35(12):325-333.

48. Manning, W. R., O. Hunter, Jr., and B. R. Powell, Jr. 1969. Elastic properties of polycrystalline yttrium oxide, dysprosium oxide, holmium oxide, and erbium oxide: Room temperature measurements. J. Amer. Ceram. Soc. 52(8):436-442.

49. Hasselman, D. P. H., and R. M. Fulrath. 1964. Effect of small fraction of spherical porosity on elastic moduli of glass. J. Amer. Ceram. Soc. 47(1):52-53.

50. Wachtman, J. B., Jr. 1969. Elastic deformation of ceramics and other refractory materials. Pages 139-168 in J. B. Wachtman, Jr., ed. Mechanical and Thermal Properties of Ceramics. National Bureau of Standards Special Publication 303.

51. Spiridinov, F. M., V. A. Stephanov, L. N. Komissarova, and V. I. Spitsyn. 1968. The binary system HfO_2-Gd_2O_3. J. Less-Common Metals 14:435-443.

52. Wilfong, R. L., L. P. Domingues, L. R. Furlong, and J. A. Finlayson. 1963. Thermal expansion of the oxides of yttrium, cerium, samarium, europium, and dysprosium. Bureau of Mines, Report of Investigation 6180.

53. Manning, W. R., O. Hunter, Jr., F. W. Calderwood, and D. W. Stacy. 1972. Thermal expansion of Nb_2O_5. J. Amer. Ceram. Soc. 55(7):342-347.

ACKNOWLEDGEMENTS

The author wishes to express his sincere appreciation to Dr. O. Hunter for his instruction and guidance, to Dr. M. F. Berard for his support, to Dr. A. E. Pasto (ORNL) for supplying the hot pressed material, to Mr. F. W. Calderwood for his assistance with the thermal expansion measurements, and to Ms. Verna Thompson for typing this report.

APPENDIX A: ELASTICITY DATA

Table A1. Identification of elasticity data used in text figures

Specimen	Composition		Figure data is plotted in	
	Mole % HfO_2	Mole % Eu_2O_3	Young's modulus	Shear modulus
0-1	0	100	4	11
0-2	0	100	4	
0-3	0	100	4	
0-4	0	100	4	11
0-A	0	100	5	
0-B	0	100		
2-A	2	98	6	
2-B	2	98		
4-A	4	96	7	
4-B	4	96		
6-A	6	94	8	11
6-B	6	94		
8-A	8	92	9	
10-A	10	90	10	
10-B	10	90		

Table A2. Elevated temperature elastic moduli of hot pressed specimen 0-1

Temp. (°C)	Young's modulus (Kbars)	Shear modulus (Kbars)
15	1301	515
180	1247	494
299	1222	
413	1204	477
528	1175	467
631	1156	
743	1129	447
817	1115	441
917	1096	434
1011	1078	423
916	1097	434
852	1111	441
762	1131	450
668	1155	459
610	1167	462
464	1198	
368	1217	481
239	1243	492
132	1271	502
20	1304	516

Table A3. Elevated temperature elastic moduli of sintered specimen 0-2

Temp. (°C)	Young's modulus (Kbars)	Shear modulus (Kbars)
25	1113	434
158	1079	420
286	1056	412
442	1037	402
607	1017	393
761	1011	389
897	1020	390
1024	1028	390
1181	1025	388
1300	1004	380
1395	980	372
1289	1007	382
1166	1039	393
1004	1076	406
867	1100	414
703	1122	420
571	1133	
394	1150	
240	1145	452
128	1125	449
16	1132	453

Table A4. Elevated temperature elastic moduli of sintered specimens 0-3 and 0-4

Temp. (°C)	Young's modulus (Kbars)	Temp. (°C)	Young's modulus (Kbars)
23	1048	25	760
137	1015	138	740
240	1000	247	727
343	988	355	713
447	966	445	701
559	941	547	689
662	926	654	678
780	921	743	668
849	913	840	657
948	902	925	646
1061	882	1020	633
1157	867	1116	621
1261	841	1212	606
1370	808	1304	591
1470	761	1401	567
1374	806	1310	596
1288	828	1202	614
1185	851	1111	627
1068	873	1011	642
951	898	909	657
849	917	815	671
751	935	711	687
650	953	615	699
564	969	500	714
437	990	402	726
335	1008	260	742
225	1024	203	749
136	1037	121	757
23	1058	16	769

Table A5. Elevated temperature elastic moduli of specimen 0-A

Sintered at 1800°C		Reheated at 1900°C	
Temp. (°C)	Young's modulus (Kbars)	Temp. (°C)	Young's modulus (Kbars)
20	1145	20	1091
172	1095	183	1054
334	1065	344	1022
460	1040	468	1000
577	1023	641	985
677	1014	798	1000
817	1013	950	1026
949	1016	1094	1045
1057	1036	1258	1038
1157	1029	1368	1016
1252	1019	1514	970
1372	994	1362	1025
1498	954	1228	1062
1384	995	1094	1095
1284	1023	944	1123
1164	1054	801	1135
1051	1081	686	1139
921	1104	544	1141
807	1126	370	1128
675	1139	177	1112
519	1155	40	1108
350	1159	15	1102
170	1147	25	1090
25	1154		

Table A6. Elevated temperature elastic moduli of specimen 0-B

Sintered at 1800°C		Reheated at 1900°C	
Temp. (°C)	Young's modulus (Kbars)	Temp. (°C)	Young's modulus (Kbars)
25	1164	25	1079
175	1122	182	1038
329	1089	350	1005
452	1072	480	987
697	1056	646	964
837	1040	799	962
980	1047	958	985
1127	1059	1104	1001
1260	1043	1261	1020
1376	1014	1373	1007
1500	972	1509	974
1407	1007	1372	1034
1313	1036	1231	1077
1211	1066	1094	1112
1095	1097	956	1138
975	1124	799	1157
832	1149	682	1168
668	1175	552	1160
516	1190	367	1155
365	1198	181	1124
183	1182	17	1120
25	1181	25	1087

Table A7. Elevated temperature elastic moduli of specimen 2-A

Sintered at 1800°C		Reheated at 1900°C	
Temp. (°C)	Young's modulus (Kbars)	Temp. (°C)	Young's modulus (Kbars)
20	1350	19	935
119	1306	184	887
276	1260	351	853
384	1240	512	845
499	1219	654	840
610	1207	809	854
715	1191	964	891
814	1180	964	903
912	1169	1111	943
1015	1162	1266	972
1115	1152	1374	988
1222	1141	1512	969
1319	1125	1377	1015
1420	1100	1235	1055
1525	1056	1101	1093
1416	1102	951	1132
1318	1134	787	1144
1214	1162	673	1148
1113	1191	540	1130
1009	1219	361	1100
903	1247	16	1032
813	1267	25	961
710	1292		
630	1314		
503	1337		
406	1353		
292	1372		
202	1380		
112	1381		
25	1363		

Table A8. Elevated temperature elastic moduli of specimen 2-B

Sintered at 1800°C		Reheated at 1900°C	
Temp. (°C)	Young's modulus (Kbars)	Temp. (°C)	Young's modulus (Kbars)
22	1399	19	967
192	1336	203	934
347	1298	356	905
460	1278	472	890
629	1247	665	865
780	1218	802	918
950	1192	959	966
1082	1170	1097	998
1245	1134	1262	1019
1380	1100	1374	1005
1518	1049	1510	979
1386	1099	1374	1023
1259	1140	1240	1061
1137	1174	1102	1100
1021	1207	958	1137
901	1236	803	1150
767	1276	679	1150
658	1302	544	1127
554	1326	355	1112
440	1352	167	1060
312	1379	20	1034
182	1399	26	947
15	1414		

Table A9. Elevated temperature elastic moduli of specimen 4-A

Sintered at 1800°C		Reheated at 1900°C	
Temp (°C)	Young's modulus (Kbars)	Temp. (°C)	Young's modulus (Kbars)
24	1483	20	918
177	1433	157	883
347	1391	345	848
525	1350	466	837
641	1312	646	837
772	1279	798	875
911	1245	952	945
1038	1214	1110	1010
1145	1186	1254	1025
1242	1157	1374	1063
1381	1113	1500	1036
1505	1055	1368	1088
1378	1113	1227	1130
1293	1146	1098	1167
1205	1176	948	1206
1094	1208	802	1234
1006	1231	673	1273
911	1269	556	1287
804	1299	369	1264
702	1328	156	1194
601	1353	20	1141
468	1391	15	1128
366	1412	245	1083
240	1438	427	1053
144	1461	623	1030
15	1493	792	1023
		951	1033
		1093	1054
		1256	1089
		1369	1077
		27	1120

Table A10. Elevated temperature elastic moduli of specimen 4-B

Sintered at 1800°C		Reheated at 1900°C	
Temp. (°C)	Young's modulus (Kbars)	Temp. (°C)	Young's modulus (Kbars)
20	1495	19	1013
82	1471	185	976
130	1457	356	945
193	1443	470	936
250	1428	645	929
304	1417	806	946
370	1402	957	990
415	1390	1098	1035
503	1371	1261	1075
551	1361	1369	1074
612	1347	1511	1034
665	1334	1370	1101
727	1318	1231	1142
777	1306	1099	1177
827	1293	950	1217
876	1280	803	1262
930	1266	687	1292
974	1254	552	1314
1037	1237	374	1326
1094	1220	168	1260
1158	1202	18	1229
1217	1183	24	1142
1270	1166	24	1111
1330	1146	24	1048
1380	1134	24	1008
1442	1103		
1259	1171		
1102	1228		
948	1272		
802	1301		
660	1345		
511	1383		
313	1472		
179	1501		
28	1510		

Table A11. Elevated temperature elastic moduli of speciman 6-A

Sintered at 1800°C		Reheated at 1900°C		
Temp. (°C)	Young's modulus (Kbars)	Temp. (°C)	Young's modulus (Kbars)	Shear
20	1516	26	1492	568
140	1475	184	1443	551
201	1460	358	1393	533
300	1436	486	1364	520
384	1414	656	1325	506
459	1396	803	1288	488
544	1376	951	1253	464
604	1363	1099	1213	454
656	1350	1262	1161	435
711	1337	1373	1121	423
770	1322	1514	1058	401
832	1306	1376	1120	423
908	1287	1234	1176	439
973	1269	1097	1220	
1050	1247	948	1258	
1120	1225	808	1317	499
1201	1200	680	1348	510
1276	1175	552	1378	522
1348	1151	375	1421	538
1418	1122	176	1467	557
1511	1073	14	1511	574
1381	1136			
1253	1181			
1100	1229			
923	1278			
750	1327			
603	1361			
483	1389			
274	1440			
143	1476			
18	1514			

Table A12. Elevated temperature elastic moduli of specimen 6-B

Sintered at 1800°C		Reheated at 1900°C	
Temp. (°C)	Young's modulus (Kbars)	Temp. (°C)	Young's modulus (Kbars)
20	1493	18	1487
160	1446	164	1430
328	1408	357	1387
470	1375	471	1360
631	1339	645	1324
800	1298	803	1287
955	1259	957	1252
1100	1220	1094	1216
1261	1172	1250	1169
1374	1134	1368	1130
1514	1054	1512	1061
1373	1131	1382	1128
1227	1180	1228	1177
1094	1219	1095	1222
944	1259	945	1266
800	1299	795	1306
673	1329	674	1339
536	1366	559	1364
369	1422	366	1410
161	1461	168	1460
15	1509	24	1488

Table A13. Elevated temperature elastic moduli of specimen 8-A

Sintered at 1800°C		Reheated at 1900°C	
Temp. (°C)	Young's modulus (Kbars)	Temp. (°C)	Young's modulus (Kbars)
20	1431	23	1504
179	1386	166	1456
362	1344	368	1408
482	1315	557	1362
622	1283	636	1343
760	1253	799	1304
919	1214	950	1266
1058	1177	1092	1225
1221	1128	1257	1167
1369	1078	1370	1125
1519	1006	1515	1052
1382	1070	1376	1127
1238	1121	1225	1198
1123	1176	1084	1238
1013	1202	943	1279
886	1236	791	1314
766	1265	648	1351
645	1292	547	1374
541	1314	367	1417
350	1371	155	1462
162	1421	23	1508
18	1464		

Table A14. Elevated temperature elastic moduli of specimen 10-A

Sintered at 1800°C		Reheated at 1900°C	
Temp. (°C)	Young's modulus (Kbars)	Temp. (°C)	Young's modulus (Kbars)
24	1559	20	1483
92	1536	169	1437
137	1521	337	1396
198	1508	456	1365
244	1496	637	1327
293	1484	795	1288
343	1471	946	1254
403	1456	1088	1218
447	1442	1249	1164
507	1428	1363	1124
579	1412	1500	1056
647	1393	1364	1121
711	1377	1223	1172
763	1364	1087	1215
814	1352	941	1256
874	1336	801	1293
918	1326	670	1325
978	1307	539	1360
1027	1295	361	1404
1094	1275	164	1455
1153	1256	18	1484
1207	1237		
1272	1216		
1323	1197		
1379	1178		
1446	1148		
1499	1116		
1549	1063		

Table A15. Elevated temperature elastic moduli of specimen 10-B

Sintered at 1800°C		Reheated at 1900°C	
Temp. (°C)	Young's modulus (Kbars)	Temp. (°C)	Young's modulus (Kbars)
20	1021	23	1398
190	989	179	1354
338	962	355	1311
459	938	478	1282
605	914	647	1244
757	890	803	1214
902	865	955	1178
1048	837	1096	1146
1205	803	1256	1099
1355	769	1373	1065
1509	718	1511	1007
1373	766	1365	1072
1226	800	1234	1116
1112	825	1101	1158
1005	850	962	1192
882	875	806	1234
763	896	690	1262
635	918	551	1290
534	934	369	1336
377	961	163	1386
163	995	25	1423
20	1028		

APPENDIX B. DENSITY AND GRAIN SIZE DATA

Table B1. Mass, dimensions, density, and average grain size of each specimen

Specimen	Mass (gm)	Thickness (cm)	Width (cm)	Length (cm)	Density (gm cm^{-3})	Average grain size (μm)
			As hot pressed			
0-1	5.8874	.1721	1.4412	3.71	7.49	6
			As sintered			
0-2	6.7077	.2103	.8328	5.07	7.55	
0-3	3.0442	.1475	.6086	4.92	6.89	
0-4	3.8602	.1662	.6425	5.56	6.51	
0-A	6.7099	.2180	.7470	5.45	7.56	117
0-B	6.2611	.2209	.6812	5.48	7.59	90
2-A	5.1871	.1788	.6781	5.51	7.76	18
2-B	7.1613	.2352	.7655	5.09	7.81	25
4-A	6.6361	.2341	.6719	5.34	7.90	14
4-B	5.2828	.1945	.6608	5.20	7.90	8
6-A	8.2967	.2505	.7432	5.63	7.92	6
6-B	7.8817	.2435	.7917	5.16	7.92	5
8-A	7.3132	.2402	.7661	5.09	7.81	
10-A	5.0911	.1880	.6505	5.24	7.94	2
10-B	7.6003	.2741	.7558	5.16	7.11	4
			As reheated			
0-A	6.0153	.2072	.7441	5.12	7.62	153
0-B	5.0236	.1962	.6743	4.98	7.62	152
2-A	3.3995	.1628	.6763	4.10	7.53	67
2-B	6.4794	.2173	.7591	5.09	7.72	76
4-A	5.6466	.2113	.6671	5.12	7.82	26
4-B	3.6211	.1495	.6267	4.95	7.81	36
6-A	6.9257	.2260	.7370	5.27	7.89	11
6-B	4.2295	.1700	.7862	4.03	7.85	10
8-A	6.4447	.2145	.7531	5.07	7.87	7
10-A	3.8885	.1601	.6370	4.88	7.81	11
10-B	5.9136	.2248	.7120	4.81	7.68	12

APPENDIX C. THERMAL EXPANSION DATA

Table C1. Percent linear thermal expansion of sintered specimens at six Eu_2O_3-HfO_2 compositions

Temp. (°C)	0 mole % HfO_2	2 mole % HfO_2	4 mole % HfO_2	6 mole % HfO_2	8 mole % HfO_2	10 mole % HfO_2
R.T.	.000	.000	.000	.000	.000	.000
50	.023	.019	.024	.022	.024	.021
100	.069	.065	.070	.068	.069	.065
150	.118	.113	.117	.122	.116	.112
200	.170	.167	.171	.173	.169	.164
250	.215	.213	.217	.223	.214	.210
300	.265	.262	.266	.274	.262	.258
350	.313	.312	.317	.325	.316	.306
400	.362	.364	.369	.375	.365	.356
450	.409	.417	.421	.424	.417	.412
500	.455	.468	.475	.475	.471	.464
550	.505	.520	.526	.524	.523	.515
600	.552	.570	.577	.574	.573	.563
650	.600	.620	.626	.626	.624	.611
700	.651	.672	.678	.677	.675	.664
750	.702	.725	.730	.729	.727	.709
800	.754	.776	.780	.783	.778	.761
850	.805	.826	.831	.837	.829	.813
900	.856	.878	.884	.892	.882	.865
950	.909	.930	.935	.946	.934	.919
1000	.959	.981	.987	1.002	.988	.972
1050	1.012	1.034	1.039	1.057	1.043	1.027
1100	1.066	1.089	1.094	1.115	1.098	1.083
1150	1.120	1.146	1.147	1.171	1.153	1.140
1200	1.172	1.202	1.207		1.210	1.195